The Astrophysical Journal, 987:91 (22pp), 2025 July 1 https://doi.org/10.3847/1538-4357/add73a

Relationships between Polycyclic Aromatic Hydrocarbons, Small Dust Grains, H_2, and H I in Local Group Dwarf Galaxies NGC 6822 and WLM Using JWST, ALMA, and the VLA

Ryan Chown[1], Adam K. Leroy[1,2], Alberto D. Bolatto[3], Jérémy Chastenet[4], Simon C. O. Glover[5], Rémy Indebetouw[6,7], Eric W. Koch[8], Jennifer Donovan Meyer[7], Nickolas M. Pingel[9], Erik Rosolowsky[10], Karin Sandstrom[11], Jessica Sutter[12], Elizabeth Tarantino[13], Frank Bigiel[14], Médéric Boquien[15], I-Da Chiang (江宜達)[16], Daniel A. Dale[17], Julianne J. Dalcanton[18,19], Oleg V. Egorov[20], Cosima Eibensteiner[7,26], Kathryn Grasha[21], Hamid Hassani[10], Hao He[14], Jaeyeon Kim[22], Sharon Meidt[4], Debosmita Pathak[1,2], Sumit K. Sarbadhicary[1,2,23], Snezana Stanimirovic[9], Vicente Villanueva[24], and Thomas G. Williams[25]
[1] Department of Astronomy, The Ohio State University, 140 West 18th Avenue, Columbus, OH 43210, USA; rchown53@gmail.com
[2] Center for Cosmology and Astroparticle Physics (CCAPP), 191 West Woodruff Avenue, Columbus, OH 43210, USA
[3] Department of Astronomy and Joint Space-Science Institute, University of Maryland, College Park, MD 20742, USA
[4] Sterrenkundig Observatorium, Universiteit Gent, Krijgslaan 281 S9, B-9000 Gent, Belgium
[5] Universität Heidelberg, Zentrum für Astronomie, Institut für Theoretische Astrophysik, Albert-Ueberle-Str 2, D-69120 Heidelberg, Germany
[6] Department of Astronomy, University of Virginia, Charlottesville, VA, USA
[7] National Radio Astronomy Observatory, Charlottesville, VA, USA
[8] Center for Astrophysics—Harvard & Smithsonian, 60 Garden Street, Cambridge, MA 02138, USA
[9] University of Wisconsin-Madison, Department of Astronomy, 475 N Charter St, Madison, WI 53703, USA
[10] Department of Physics, University of Alberta, 4-183 CCIS, Edmonton, Alberta, T6G 2E1, Canada
[11] Department of Astronomy & Astrophysics, University of California, San Diego, 9500 Gilman Drive, La Jolla, CA 92093, USA
[12] Whitman College, 345 Boyer Avenue, Walla Walla, WA 99362, USA
[13] Space Telescope Science Institute, 3700 San Martin Drive, Baltimore, MD 21218, USA
[14] Argelander-Institut für Astronomie, Universität Bonn, Auf dem Hügel 71, 53121 Bonn, Germany
[15] Université Côte d'Azur, Observatoire de la Côte d'Azur, CNRS, Laboratoire Lagrange, 06000, Nice, France
[16] Institute of Astronomy and Astrophysics, Academia Sinica, No. 1, Sec. 4, Roosevelt Road, Taipei 106216, Taiwan
[17] Department of Physics and Astronomy, University of Wyoming, Laramie, WY 82071, USA
[18] Center for Computational Astrophysics, Flatiron Institute, 162 Fifth Ave, New York, NY 10010, USA
[19] Department of Astronomy, University of Washington, Seattle, WA 98195, USA
[20] Astronomisches Rechen-Institut, Zentrum für Astronomie der Universität Heidelberg, Mönchhofstr. 12–14, D-69120 Heidelberg, Germany
[21] Research School of Astronomy and Astrophysics, Australian National University, Canberra, ACT 2611, Australia
[22] Kavli Institute for Particle Astrophysics & Cosmology (KIPAC), Stanford University, CA 94305, USA
[23] Department of Physics, The Ohio State University, Columbus, OH 43210, USA
[24] Departamento de Astronomía, Universidad de Concepción, Barrio Universitario, Concepción, Chile
[25] Sub-department of Astrophysics, Department of Physics, University of Oxford, Keble Road, Oxford OX1 3RH, UK
Received 2025 April 10; revised 2025 May 8; accepted 2025 May 9; published 2025 July 1

Abstract

We present 0.6–3.2 pc resolution mid-infrared (MIR) JWST images at 7.7 μm (F770W) and 21 μm (F2100W) covering the main star-forming regions of two of the closest star-forming low-metallicity dwarf galaxies, NGC 6822 and Wolf–Lundmark–Melotte (WLM). The images of NGC 6822 reveal filaments, edge-brightened bubbles, diffuse emission, and a plethora of point sources. By contrast, most of the MIR emission in WLM is pointlike, with a small amount of extended emission. Compared to solar-metallicity galaxies, the ratio of 7.7 μm intensity ($I_\nu^{\rm F770W}$), tracing polycyclic aromatic hydrocarbons (PAHs), to 21 μm intensity ($I_\nu^{\rm F2100W}$), tracing small, warm dust grain emission, is suppressed in these low-metallicity dwarfs. Using Atacama Large Millimeter/submillimeter Array CO(2–1) observations, we find that detected CO intensity versus $I_\nu^{\rm F770W}$ at $\approx$2 pc resolution in dwarfs follows a similar relationship to that at solar metallicity and lower resolution, while the CO versus $I_\nu^{\rm F2100W}$ relationship in dwarfs lies significantly below that derived from solar-metallicity galaxies at lower resolution, suggesting more pronounced destruction of CO molecules at low metallicity. Finally, adding in Local Group L-Band Survey 21 cm H I observations from the Very Large Array, we find that $I_\nu^{\rm F2100W}$ and $I_\nu^{\rm F770W}$ versus total gas ratios are suppressed in NGC 6822 and WLM compared to solar-metallicity galaxies. In agreement with dust models, the level of suppression appears to be at least partly accounted for by the reduced galaxy-averaged dust-to-gas and PAH-to-dust mass ratios in the dwarfs. Remaining differences are likely due to spatial variations in dust model parameters, which should be an exciting direction for future work in local dwarf galaxies.

Unified Astronomy Thesaurus concepts: Dwarf irregular galaxies (417); Polycyclic aromatic hydrocarbons (1280); Interstellar dust (836); Dust nebulae (413); Molecular gas (1073); Interstellar atomic gas (833)

[26] Jansky Fellow of the National Radio Astronomy Observatory.

1. Introduction

Low-metallicity star-forming regions (hereafter "SF regions") are common in outer disks of galaxies like the Milky Way, in dwarf galaxies, and at high redshifts

(R. Maiolino & F. Mannucci 2019). The low metallicity in these regions influences the star formation process and interstellar medium (ISM) conditions. Metallicity (Z) governs the abundances of dust and ISM coolants—including CO, the most widely used molecular gas tracer (A. D. Bolatto et al. 2013). This, in turn, affects the balance between atomic and molecular gas (S. C. O. Glover & P. C. Clark 2012a; F. Galliano et al. 2018; A. Saintonge & B. Catinella 2022).

The nearest accessible extragalactic low-Z SF regions are found in dwarf galaxies,[27] which have low total masses, high H I mass fractions, low dust-to-gas mass ratios (DGRs), harder radiation fields, and lower molecular-to-total hydrogen ratios compared to the metal-rich (e.g., solar-metallicity) massive star-forming galaxies (for a review see D. A. Hunter et al. 2024).

While we have theoretical predictions of the structure and physical state of the gas in low-Z SF regions (S. C. O. Glover & P. C. Clark 2012b; C.-Y. Hu et al. 2021, 2023; C.-G. Kim et al. 2024), observations that test these predictions have been challenging (see summary by D. A. Hunter et al. 2024). To a large extent, this reflects the fact that measuring the amount of H_2 in low-Z SF regions is challenging. Millimeter-wavelength rotational line emission from carbon monoxide (CO), the most widely used tracer of H_2, becomes faint at low metallicity (P. Maloney & J. H. Black 1988; I. A. Grenier et al. 2005; M. G. Wolfire et al. 2010; S. C. O. Glover & P. C. Clark 2012a; A. Schruba et al. 2012; A. D. Bolatto et al. 2013; S. C. Madden et al. 2020). At solar metallicity ($Z = Z_\odot$), dust shields CO from dissociating far-ultraviolet radiation, whereas at $Z \leqslant 0.3\,Z_\odot$, CO is preferentially dissociated relative to H_2, which self-shields much more effectively (S. C. Madden et al. 2020). As a result, low-metallicity molecular clouds are expected to harbor significant amounts ($\gtrsim$70%; S. C. Madden et al. 2020) of H_2 that is not traceable by CO (i.e., it is "CO-dark"; P. Maloney & J. H. Black 1988; I. A. Grenier et al. 2005; M. G. Wolfire et al. 2010; S. C. O. Glover & P. C. Clark 2012a). At very low metallicities (about $0.1\,Z_\odot$ or lower) up to 100% of the H_2 mass may be CO-dark (e.g., Y. Shi et al. 2016; S. C. Madden et al. 2020; Y. Shi et al. 2020).

Attempting to measure the amount and properties of CO-dark H_2 is an active area of research. Spectroscopy of multiple carbon species (e.g., J. L. Pineda et al. 2017; K. E. Jameson et al. 2018), dynamical measurements based on the detected CO, UV absorption or IR emission tracing H_2 directly, and even gamma rays all offer possible routes forward (see review by A. D. Bolatto et al. 2013). Perhaps the most widely used approach is to use observations of dust to trace the gas (e.g., F. P. Israel 1997; A. K. Leroy et al. 2011). This approach assumes that dust and gas are well mixed, and leverages the fact that dust is often still visible in emission even at low Z.

Spatial resolution has been a major obstacle to using dust to trace H_2 in dwarf galaxies. Far-IR telescopes have had limited angular resolution (e.g., Herschel had FWHM $\approx$13″ near the peak of the IR spectral energy distribution (SED) at 160 μm) and the molecular clouds in dwarf galaxies tend to be small (e.g., M. Rubio et al. 2015; A. Schruba et al. 2017; Y. Shi et al. 2020). JWST can map mid-IR (MIR) emission at much higher resolution, $\sim$0.″3–1″, offering the prospect to push dust studies of low-Z SF regions into a new era, even resolving clouds in the Local Group where $1'' \lesssim 5$ pc.

To help take this next step, we present new JWST MIRI imaging of MIR dust emission from five low-Z SF regions in two Local Group galaxies, NGC 6822 and the Wolf–Lundmark–Melotte (WLM) galaxy (Table 1). Along with NGC 2366 (M. S. Oey et al. 2017) and Sextans B (Y. Shi et al. 2020), NGC 6822 (A. Schruba et al. 2017) and WLM (M. Rubio et al. 2015) are the only low-Z galaxies beyond the Small Magellanic Cloud (SMC) where CO emission has been detected and resolved into individual clouds and cores (D. A. Hunter et al. 2024). Therefore, these regions harbor reservoirs of molecular gas in addition to signatures of recent high-mass star formation.

An important difference from previous efforts using dust to trace CO-dark H_2 is that JWST observes the MIR. The MIR is dominated by continuum emission from stochastically heated small dust grains and a number of strong, broad emission features produced by the stretching and bending modes of polycyclic aromatic hydrocarbons (PAHs; L. J. Allamandola et al. 1989; B. T. Draine & A. Li 2007; A. G. G. M. Tielens 2008; B. T. Draine 2011; F. Galliano et al. 2018; N. Li et al. 2020; B. S. Hensley et al. 2022; B. S. Hensley & B. T. Draine 2023). Neither MIR continuum nor PAH emission directly traces the total dust mass in the same way as the optical depth derived from the SED (e.g., F. Galliano et al. 2018), but PAH and stochastic emission from small dust grains is expected to trace the product of gas column density, the intensity of the interstellar radiation field, and the small grain abundance. In more massive galaxies, there are strong correlations between this MIR dust emission and CO emission on scales as large as whole galaxies and as small as molecular clouds (e.g., Y. Gao et al. 2019; R. Chown et al. 2021, 2025a; A. K. Leroy et al. 2021, 2023; K. M. Sandstrom et al. 2023; C. M. Whitcomb et al. 2023a; V. Villanueva et al. 2025).

This work aims to explore how the use of MIR emission to trace gas extends to low-Z SF regions. Except for a pioneering study by P. Gratier et al. (2010), this relationship is mostly unexplored in low-Z galaxies. One clear issue is variations in PAH abundance. Compared to massive, metal-rich galaxies, low-Z galaxies exhibit low PAH abundances as traced by both SED fitting and the ratio of PAH emission to small dust grain emission (C. W. Engelbracht et al. 2005; D. W. Hogg et al. 2005; S. C. Madden et al. 2006; B. T. Draine et al. 2007; K. D. Gordon et al. 2008; A. Li 2020; J. Chastenet et al. 2025). This reflects some combination of enhanced PAH destruction and reduced PAH production at low Z. Resolved mapping of PAH abundances in the Magellanic Clouds suggested an overall drop in PAH abundance near the metallicity of the SMC, enhanced PAH abundance in molecular gas-dominated regions, and suppressed PAH abundance in H II regions (K. M. Sandstrom et al. 2010; J. Chastenet et al. 2019). JWST allows similar resolved measurements beyond the Magellanic Clouds for the first time. With these goals in mind we address the following questions.

1. How does the ratio of PAH emission to small dust grain emission—a proxy for the PAH-to-dust mass fraction—vary across these regions? In particular, how does this ratio vary between H II regions and the surrounding molecular clouds? How do the ratios compare between the low-metallicity NGC 6822, the very low-metallicity WLM, and more massive, metal-rich galaxies?

[27] Throughout this work, by "dwarf galaxies" or "dwarfs" we mean "dwarf irregulars" as opposed to dwarf galaxies with little to no interstellar medium, e.g., dwarf spheroidals.

Table 1
Target Galaxy Properties

Property	NGC 6822	Reference	WLM	Reference
Hubble type	IB(s)m	NED[a]	IB(s)m	NED
R.A. (J2000)	$19^h44^m55\overset{s}{.}74$	NED	$00^h01^m58\overset{s}{.}1610$	NED
Decl. (J2000)	$-14^d48^m12\overset{s}{.}4$	NED	$-15^d27^m39\overset{s}{.}340$	NED
Distance (kpc)	474 ± 13	J. A. Rich et al. (2014)	985 ± 33	R. Leaman et al. (2012)
$Z/Z_\odot$[b]	0.2	L. Hernández-Martìnez et al. (2009)	0.13	H. Lee et al. (2005)
$M_*/M_\odot$	1.5×10^8	S. C. Madden et al. (2013)	1.6×10^7	H.-X. Zhang et al. (2012)
$M_{HI}/M_\odot$	1.3×10^8	D. T. F. Weldrake et al. (2003)	$(3.2 \pm 0.3) \times 10^7$	D. C. Jackson et al. (2004)
DGR[c]	$\approx 2.0 \times 10^{-3}$	A. Schruba et al. (2017)	$\approx 1 \times 10^{-3}$	A. Rémy-Ruyer et al. (2014)
SFR/$M_\odot$ yr^{-1}	0.015	B. V. Efremova et al. (2011)	0.006	D. A. Hunter et al. (2010)
$\alpha_{CO}/\alpha_{CO,MW}$[d]	31	Equation (1)	60	Equation (1)
rms noise in F770W images at varying resolutions (MJy sr^{-1})				
Native	0.062		0.041	
0.″9	0.022		0.010	
2.″0	0.019		0.007	
rms noise in F2100W images at varying resolutions (MJy sr^{-1})				
Native	0.283		0.233	
0.″9	0.085		0.058	
2.″0	0.059		0.025	

Notes.
[a] NASA/IPAC Extragalactic Database.
[b] Total gas-phase oxygen abundance in H II regions, converted to Z assuming $12 + \log(O/H) = \log_{10}(Z/Z_\odot) + 8.73$ dex. Note that we expect region-to-region variations in Z (e.g., as in the SMC/LMC, S. Choudhury et al. 2016, 2018) but lack measurements for each region.
[c] For NGC 6822 we show 1/GDR (GDR is the gas-to-dust ratio) from Table 1 of A. Schruba et al. (2017), where the dust mass is from A. Rémy-Ruyer et al. (2015) and the gas mass is from D. T. F. Weldrake et al. (2003) and P. Gratier et al. (2010). For WLM we use the broken power-law prescription for GDR assuming $Z = 0.13\ Z_\odot$ and a metallicity-dependent CO-to-H_2 conversion factor (Table 1 of A. Rémy-Ruyer et al. 2014). We also use this broken power law to estimate DGR for PHANGS (Section 3.5).
[d] CO-to-H_2 conversion factor relative to the Milky Way value $\alpha_{CO,MW} = 4.35\ M_\odot\ pc^{-2}\ (K\ km\ s^{-1})^{-1}$, computed via Equation (1).

2. In the regions that do show CO emission, how does the CO emission observed by Atacama Large Millimeter/submillimeter Array (ALMA) correlate with the PAH and small dust grain emission ratios? How do the normalization and strength of these correlations compare to those found in massive, high-metallicity galaxies?
3. How do PAH and small dust grain emission correlate with ISM tracers, especially the atomic gas traced by 21 cm mapping, over the full field of our images? Is there evidence for a phase dependence of the small grain or PAH abundance?

We describe our new observations and supporting data in Section 2, address these questions Section 3, and summarize our conclusions in Section 4. In the Appendix we connect our MIR band ratios to dust model parameters and discuss implications.

2. Data

2.1. New JWST 7.7 and 21 μm Observations

As part of Cycle 2 GO program #4256, we used JWST MIRI to image four star-forming complexes in NGC 6822 and one in WLM (Figure 1). CO(2–1) emission has been resolved and detected in each of these regions using ALMA (Section 2.2). The complexes collectively capture most of the star formation activity in both galaxies. Fields 1 (Hubble X), 2 (Hubble V), 3 (Hubble I/III), and 4 (Hubble IV) collectively account for ≈2/3 of the global Hα and Spitzer 24 μm fluxes in NGC 6822 (A. Schruba et al. 2017).

The observations occurred on 2023 October 19 and November 1. We observed each field using the F770W and F2100W filters and a 2 × 1 pointing mosaic, which covered the CO and mid-IR emission known from previous observations (J. M. Cannon et al. 2006), and most of the associated Hα emission (D. A. Hunter et al. 2012; A. Schruba et al. 2017). We used the FASTR1 readout pattern, with 20 groups per integration and a four-point dither. The F770W observations were made with one integration per exposure, while F2100W ones were made with two integrations per exposure. We observed one off-galaxy field each for NGC 6822 and WLM, and used this to construct a background that we subtracted from each on-source field. The total exposure times for each 2 × 1 field mosaic were 444 s for F770W and 910 s for F2100W. The corresponding per-point exposure times were therefore 222 s for F770W and 455 s for F2100W.

The resolution of JWST is 0.″269 at F770W and 0.″674 at F2100W. At the distance of NGC 6822 (Table 1), the corresponding linear resolutions are 0.62 pc (F770W) and 1.55 pc (F2100W), while for WLM this corresponds to linear resolutions of 1.28 pc (F770W) and 3.22 pc (F2100W). The ≈200″ × 125″ extent of our mosaics corresponds to an areal coverage of ≈500 pc × 300 pc for NGC 6822 and ≈950 pc × 600 pc for WLM.

The data were reduced using the PHANGS-JWST pipeline (`pjpipe`, T. G. Williams et al. 2024) version 1.2.0, JWST pipeline (`jwst`) version 1.17.1 (H. Bushouse et al. 2025), and

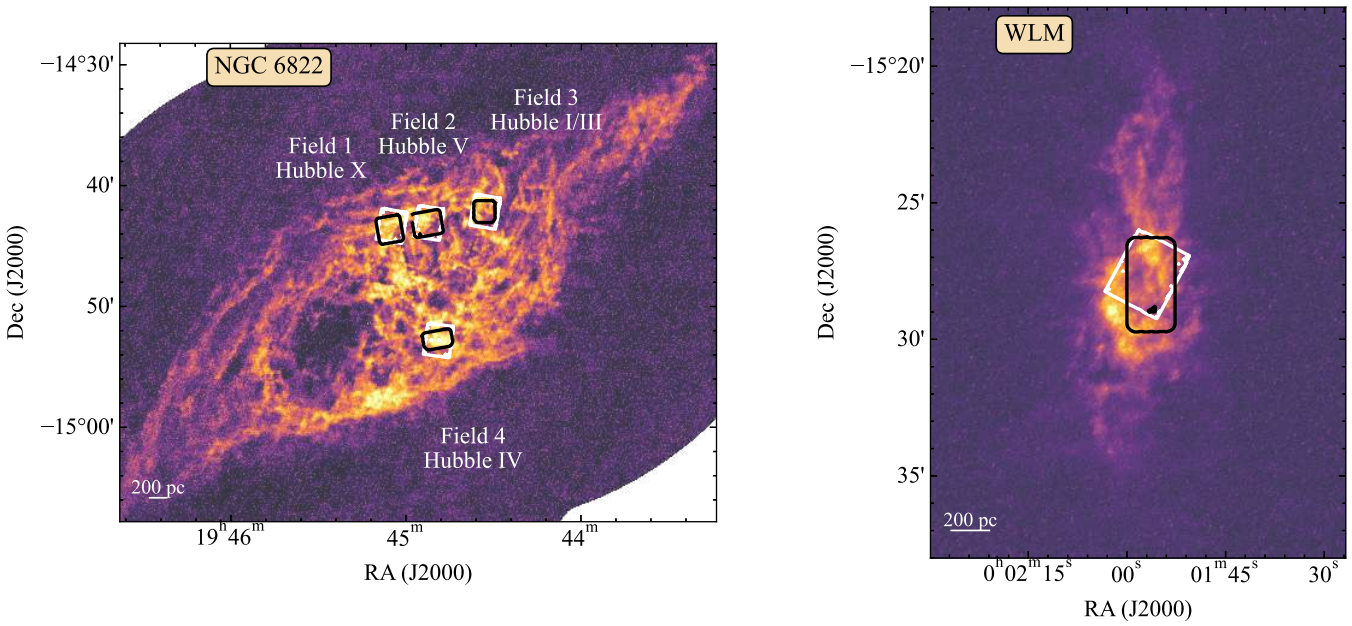

Figure 1. 4″21 cm H I peak intensity image from the Local Group L-Band Survey (E. Koch et al. 2025, in preparation; N. M. Pingel et al. 2024; N. Pingel et al. 2025, in preparation). Contours show the footprints of our JWST MIRI observations (white) and ALMA CO(2–1) data (black).

CRDS context `1322.pmap`. Compared to the current default observatory pipeline, `pjpipe` implements improved solutions for matching backgrounds between different tiles of the mosaics and improves the astrometric alignment between dithers and adjacent tiles. We find that individual exposures in dither sequences show varying background levels. The origins of these offsets may be due to persistence (J. E. Morrison et al. 2023; D. Dicken et al. 2024), but at the time of writing this is not completely certain. These offsets present a challenge for this data set in particular because the targeted regions show faint extended emission with surface brightness $I_\nu \approx 0.1$ MJy sr^{-1}, while the individual exposures can differ by a similar amount in overlapping areas. This problem is more significant for the F2100W observations, where the backgrounds are much brighter than for F770W (J. Rigby et al. 2023). We use the `skymatch` step of the JWST pipeline with `method=local`, which helps to make the overall flux level of exposures and adjacent pointings more uniform. We estimate the uncertainty on the overall intensity level to be about 0.1 MJy sr^{-1}.

In order to compare the JWST bands to one another and to other data with different point-spread functions (PSFs), we convolve the maps to several resolutions. We construct kernels that convert from JWST PSFs generated using `webbpsf`[28] to a series of Gaussian PSFs with different FWHMs. We construct versions of the JWST maps with FWHM 0.″9 (≈2.1 pc at NGC 6822 and 4.3 pc at WLM). As discussed by T. G. Williams et al. (2024), this represents the sharpest Gaussian PSF to which the F2100W data can be safely convolved, and this convolution decreases the noise of F2100W images by a factor of about ≈3. We also create versions of the maps at the 2″ (≈4.7 pc or 9.6 pc) working resolutions of the ALMA CO data (see Section 2.2) and the 7.″5 (NGC 6822) and 8.″25 (WLM) resolutions of the Very Large Array (VLA) 21 cm maps (Section 2.3).

[28] https://stpsf.readthedocs.io; 1.4.0.

The noise level in the maps depends on resolution. Table 1 reports the statistical noise in each filter at several resolutions, gauged from apparently signal-free regions of the images (the rms noise reported for NGC 6822 is the average of the rms noise levels in Fields 1–4). The native resolution JWST images are hosted at the Canadian Advanced Network for Astronomical Research (R. Chown et al. 2025b).

2.2. ALMA CO(2–1)

We compare MIR emission to ALMA CO(2–1) data. For WLM these are from ALMA project 2018.1.00337.S (PI Rubio). They have been published by H. N. Archer et al. (2024) and will be presented by M. Rubio et al. (2025, in preparation). For NGC 6822 we use the CO(2–1) data from A. Schruba et al. (2017) for Field 3. For Fields 1, 2, and 4 we use new CO(2–1) mapping from project 2024.1.01179.S (PI Chown). These new data cover approximately the same area as the A. Schruba et al. (2017) mapping of these fields but achieve ≈3–4× better sensitivity. This project will eventually include data with short and zero spacing, but these are still being observed. Here we use the observatory-delivered main array (12 m) imaging only. In both galaxies, the CO mosaics approximately match the coverage of our JWST data. We convolve the data to have round synthesized beams of 1.″35 for NGC 6822 Field 1, 1.″2 for Field 2, 1.″1 for Fields 3 and Field 4, and 2″ for WLM. The maximum recoverable angular scale is 11″ for NGC 6822 and 16″ for WLM.

We produce integrated intensity maps at the native, 2″ (FWHM) resolution, and resolution matched to the 21 cm data. To do this, we integrated over a velocity range of ±8.4 km s^{-1} around the local mean 21 cm velocity. The 21 cm line is detected everywhere in our fields and its velocity typically aligns well with the velocity of CO emission (e.g., A. Schruba et al. 2011). We arrived at the ±8.4 km s^{-1} window by inspecting the CO cubes by eye and determining that the observed bright CO emission lies within this velocity range. After convolution to a matched 2″ resolution, the resulting integrated intensity maps have typical

uncertainties of $1\sigma \approx 0.1$ K km s^{-1} for NGC 6822 Fields 1 and 2, $\approx$0.4 K km s^{-1} for NGC 6822 Field 3, and $\approx$0.15 K km s^{-1} for Field 4 and WLM.

We analyze the integrated intensity of CO(2–1) rather than H_2 surface density except for Section 3.5, where we combine CO and H I measurements to calculate total H column densities. To do this, we employ CO-to-H_2 conversion factors, α_{CO}, that assume a scaling with metallicity (following E. Schinnerer & A. K. Leroy 2024):

$$\alpha_{CO} = \alpha_{CO,MW}(Z/Z_{\odot})^{-1.5}, \quad (1)$$

using Z in Table 1 (also see T. G. Bisbas et al. 2025). This yields α_{CO} of 134 and 261 $M_{\odot}$ pc^{-2} (K km s^{-1})$^{-1}$ for NGC 6822 and WLM respectively.

2.3. VLA 21 cm

Neutral atomic hydrogen (H I) makes up most of the ISM in these galaxies. To trace this gas we use new VLA maps of the 21 cm line from the "Local Group L-Band Legacy Survey[29]" (LGLBS; E. Koch et al. 2025, in preparation) and imaged as described by N. M. Pingel et al. (2024). We use 21 cm images that combined data from all four VLA configurations and the short-spacing data from the Green Bank Telescope. These images appear in Figure 1. We convolve both VLA data cubes to have a circular synthesized beam, which has FWHM 7.″5 for NGC 6822 and 8.″25 for WLM. We created line-integrated intensity masks for each field and converted these to column density assuming optically thin 21 cm emission.[30] The typical 1σ sensitivity of N(H I) column density of these maps is $<5 \times 10^{19}$ cm^{-2}, and 21 cm emission is detected at good significance along all sight lines in our fields.

2.4. Hα

We use Hα images to estimate the boundaries of the H II region in each field. Fields 1–3 in NGC 6822 were observed using the SITELLE optical integral field unit at the Canada–France–Hawaii Telescope as part of the SIGNALS survey (L. Rousseau-Nepton et al. 2019), and narrowband Hα maps for all four NGC 6822 fields and WLM were obtained as part of the LITTLE THINGS survey (D. A. Hunter et al. 2012). To be consistent across fields, we use the LITTLE THINGS narrowband images when analyzing Hα intensity measurements, but use SIGNALS where available for the visualizations in Figures 2 and 3. The map units for the LITTLE THINGS data were converted to flux from native units of counts by applying calibration factors available on the LITTLE THINGS website.[31] The seeing for the LITTLE THINGS Hα data is 2.″5 for NGC 6822 and 3.″2 for WLM (D. A. Hunter & B. G. Elmegreen 2004). Further details of the LITTLE THINGS Hα data are given by D. A. Hunter & B. G. Elmegreen (2004).

2.5. Comparison Data

We compare our measurements for NGC 6822 and WLM to similar measurements for more massive galaxies at coarser resolution as well as to similar measurements of the Magellanic Clouds obtained with Spitzer.

2.5.1. Massive Galaxies from PHANGS

We compare our measurements to F770W, F2100W, CO(2–1), H I, and Hα observations of star-forming regions obtained by the PHANGS surveys (see A. K. Leroy et al. 2021). We use F770W and F2100W observations from PHANGS-JWST (J. C. Lee et al. 2023, Cycle 1 GO program #2107). The processing for those data is described by T. G. Williams et al. (2024), and we use public release version v1.0.1 (T. Williams et al. 2023). The CO(2–1) observations come from PHANGS–ALMA (A. K. Leroy et al. 2021). The extinction-corrected Hα measurements are from PHANGS-MUSE (E. Emsellem et al. 2022), and the identifications of nebulae in PHANGS-MUSE are from B. Groves et al. (2023). The 21 cm data come from the compilations described by J. Sun et al. (2020, 2022) and I.-D. Chiang et al. (2024).

Currently, the matched data described above exist for 19 galaxies, which form our working comparison data set. Except for the 21 cm data, most data have angular resolution in the range $\approx$0.″8–1.″5, which corresponds to a common physical resolution of $\approx$100–150 pc at the distances to the galaxies. To form our comparison measurements, we convolve the ALMA, JWST, and MUSE data to the common angular resolution achievable for all three data sets for each galaxy. Then we project the maps to a common astrometric grid with Nyquist sampled pixels (i.e., pixel size = FWHM/2) at this working resolution, and measure the intensities for each band at each location in each galaxy. We use the nebular regions defined by B. Groves et al. (2023) as a mask and use this to identify each pixel as containing mostly emission from diffuse or nebular regions. We note that the physical resolution is $\approx$50 times more coarse than our JWST observations of NGC 6822 and WLM, and so the delineation between "inside" and "outside" H II regions (Section 3.2) is not as clean for PHANGS (O. V. Egorov et al. 2023; J. Sutter et al. 2024). We sample the 21 cm intensities and corresponding H I column densities at their native resolution, which is much coarser than the other data (typically $\gtrsim 10'' \sim 1$ kpc).

The properties of these 19 galaxies are reported by A. K. Leroy et al. (2021), E. Emsellem et al. (2022) and J. C. Lee et al. (2023). In our comparisons, we highlight the two lowest-mass targets within these 19 galaxies, which offer an intermediate case between the more massive typical PHANGS targets and our dwarf galaxy targets. IC 5332 is a low-mass spiral with $\log_{10}(M_{\star}/M_{\odot}) = 9.67$, $\log_{10}(\mathrm{SFR}/M_{\odot}\ \mathrm{yr}^{-1}) = -0.39$, and $12 + \log_{10}(\mathrm{O/H}) = 8.30$ dex at r_{eff} while NGC 5068 is a barred low-mass spiral with $\log_{10}(M_{\star}/M_{\odot}) = 9.40$, $\log_{10}(\mathrm{SFR}/M_{\odot}\ \mathrm{yr}^{-1}) = -0.56$, and $12 + \log_{10}(\mathrm{O/H}) = 8.32$ dex at r_{eff} (see A. K. Leroy et al. 2021; B. Groves et al. 2023).

2.5.2. The Magellanic Clouds

At 49.6 kpc (G. Pietrzyński et al. 2019) and 62 kpc (R. de Grijs & G. Bono 2015; V. Scowcroft et al. 2016), the LMC and SMC are by far the closest low-mass star-forming galaxies. Their proximity means that previous-generation IR telescopes match the physical resolution achieved by JWST in our more distant Local Group targets. We compare our JWST F770W and F2100W measurements to Spitzer 8 μm and 24 μm

[29] www.lglbs.org

[30] N. M. Pingel et al. (2024) show that opacity can be significant within the star-forming complexes in NGC 6822, but we lack a method to correct the H I over each whole field. We expect the largest opacities to be present in the regions of high column density near the centers of the complexes.

[31] E.g. http://www2.lowell.edu/users/dah/littlethings/wlm.html for WLM.

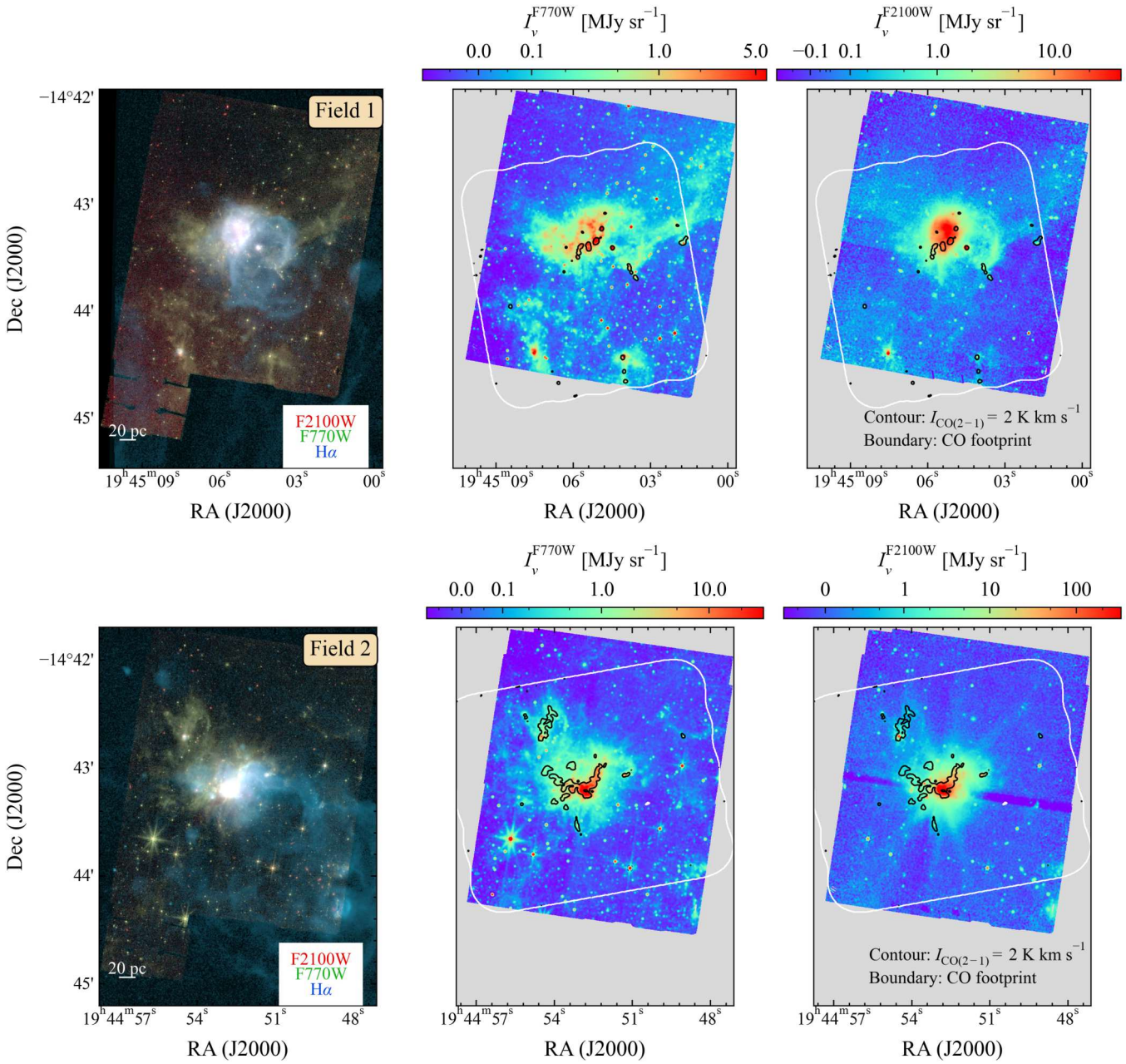

Figure 2. Left: images of Fields 1 (top) and 2 (bottom) in NGC 6822 combining JWST F2100W (red), JWST F770W (green), and Hα (blue) from SIGNALS. Middle and right: the F770W and F2100W maps from JWST at 0.″9 resolution. The white boundary shows the field of view of ALMA CO(2–1) mapping (Section 2.2), and the black contours show where CO is detected at $\approx 10\sigma$ at native resolution. The diffraction spikes are artifacts around point sources in both F770W and F2100W. Note how MIR emission is detected over a much more extended area than CO.

measurements of the LMC from SAGE (M. Meixner et al. 2006) and of the SMC from SAGE-SMC (K. D. Gordon et al. 2011). We use the publicly available maps whose processing is described in the survey papers, with additional processing as described by J. Chastenet et al. (2019). J. Chastenet et al. (2019) conducted a careful background subtraction and beam-matched all data at the $\approx 6''$ resolution of Spitzer's MIPS 24 μm filter ($\approx$1.4 pc and 1.8 pc at the distance to the LMC and SMC). To identify which regions of the galaxy correspond to star-forming H II regions similar to our target fields, we use Hα images of the LMC and SMC from the Southern Hα Sky Survey Atlas (SHASSA; J. E. Gaustad et al. 2001), which has $48''$ ($\approx$12 pc and 14 pc) pixels.

3. Results

Figures 2 through 4 show our new JWST F770W and F2100W images. We detected extended emission in both filters in all four NGC 6822 fields. Field 3 shows a striking shell structure that resembles the infrared bubbles identified in the SMC (W. G. Ji et al. 2012) and Milky Way (E. Churchwell et al. 2004, 2006; M. S. Povich et al. 2007; C. Watson et al. 2009; R. J. Simpson et al. 2012; T. Jayasinghe et al. 2019). Meanwhile, Fields 2 and 4 both show compact, bright MIR emission that is coincident with the brightest CO emission in the galaxy, perhaps consistent with an early evolutionary state (A. Schruba et al. 2017).

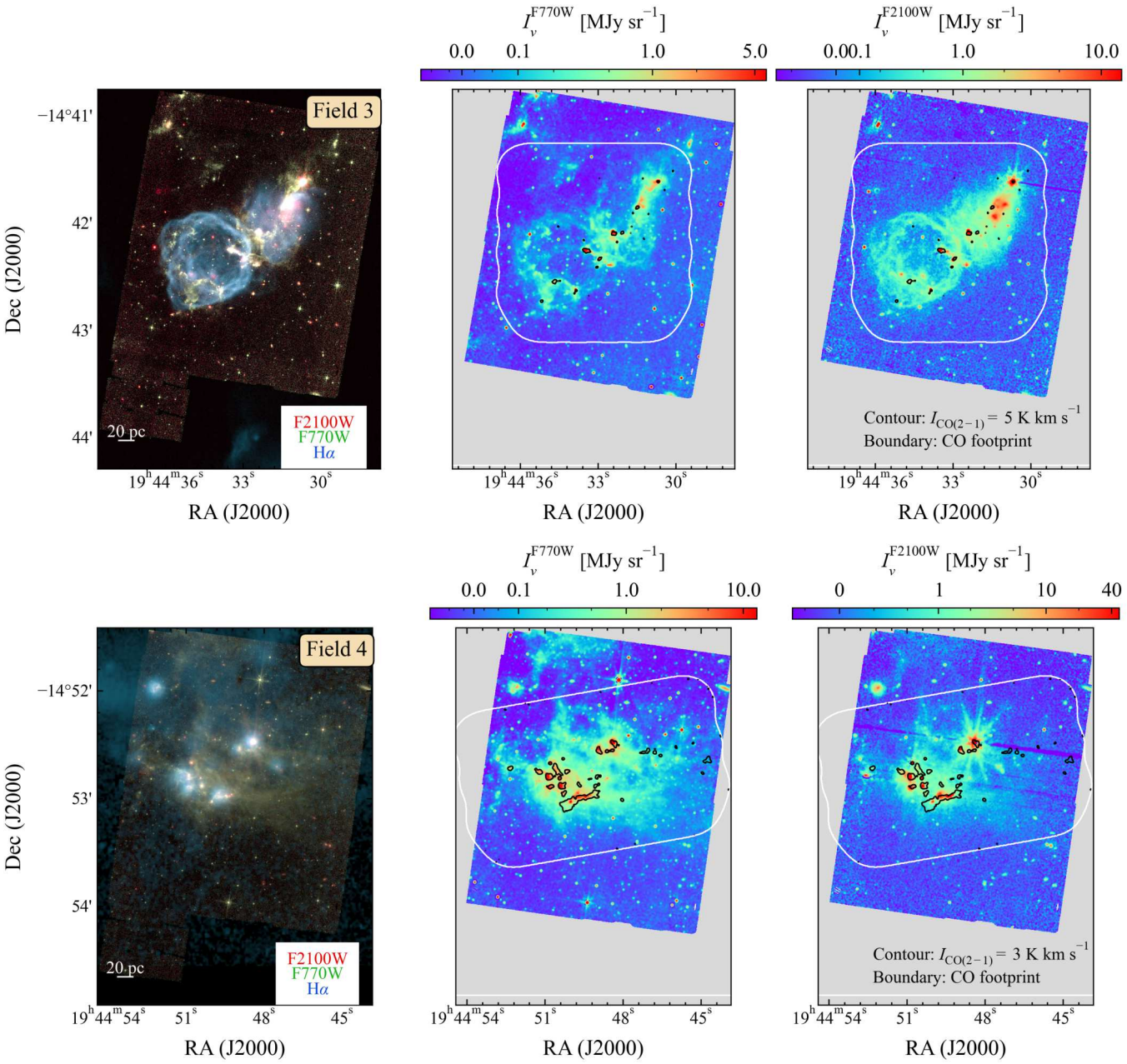

Figure 3. As Figure 2 but for NGC 6822 Fields 3 (top) and 4 (bottom). In Field 4 the Hα data come from D. A. Hunter et al. (2012).

The morphology of MIR emission in WLM (Figure 4) appears fainter and much less extended than that in NGC 6822. This likely reflects WLM's lower metallicity, $Z \approx 0.13\,Z_\odot$ compared to $Z \approx 0.2\,Z_\odot$ in NGC 6822. The striking difference in MIR morphology may reflect the fact that the PAH abundance and dust-to-gas ratio drop sharply over this metallicity range (see reviews by F. Galliano et al. 2018; N. Li et al. 2020; D. A. Hunter et al. 2024).

In more detail, the images show:

1. Though the F770W and F2100W images appear overall similar, the median $I_\nu^{F770W}/I_\nu^{F2100W}$ ratio varies from field to field and appears lower in regions with the bright Hα emission. We measure these variations and discuss their implications for variations in PAH abundance in Section 3.2.
2. In NGC 6822, bright, compact dust emission appears associated with detected CO emission. We also see extended, lower-intensity MIR dust emission surrounding these bright regions. This likely reflects some combination of CO-faint molecular gas, cold atomic gas, and the impact of dust heating by the nearby massive stars. We compare CO and MIR emission in Section 3.4.
3. Fainter diffuse MIR emission located far from the CO detections is visible in all four NGC 6822 fields. This may be dust associated with atomic gas clouds. Given the pervasive nature of the H I it is just as remarkable that we do *not* detect MIR emission along each line of sight, implying that much of the diffuse ISM may have a low abundance of dust and PAHs. We compare MIR emission, H I, and total gas column density, N(H), in Section 3.5.

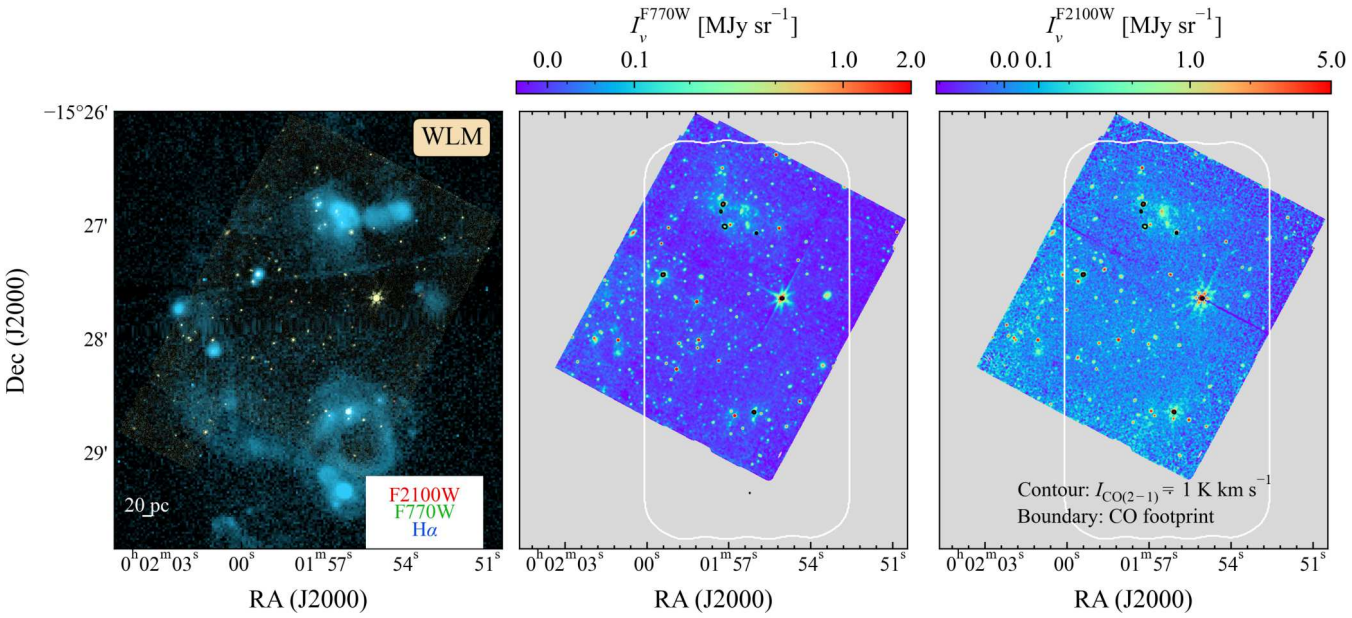

Figure 4. As Figure 2 but for WLM. The Hα here comes from D. A. Hunter et al. (2012).

In addition to the dust, many point sources are visible in the images. We discuss their effect on our measurements in Section 3.1.

3.1. Impact of MIR Point Sources

Our images show a large number of point sources. Many of these are MIR-bright or foreground stars, including young stellar objects (YSOs; e.g., O. C. Jones et al. 2023; C. Nally et al. 2024). Some may be young clusters. There are also a handful of background galaxies. Our analysis focuses on dust emission, so stars and background galaxies represent contaminants. To deal with these, we first mask bright sources that appear unrelated to our target galaxies, either because they are clearly background galaxies or because they appear to be foreground stars. We do this by hand. These regions remain masked throughout our analysis.

After masking the bright sources, numerous fainter point sources remain. We attempted to identify and mask these based on F770W/F2100W colors, but this approach proved unreliable and we have deferred it to future work. We choose not to mask these fainter sources because distinguishing them from the extended, structured diffuse MIR emission that is the focus of our analysis presents significant challenges. Instead we use blank sky regions in each of the native-resolution F770W and F2100W images to estimate the mean surface brightness due to faint point sources. We manually select regions in each field that show no diffuse MIR emission.[32] Then we run `SExtractor` (E. Bertin & S. Arnouts 1996) on each image. Within each control region we calculate the mean surface brightness of point sources over the whole region via

$$\langle I_\nu^{\rm ptsrc}\rangle_{\rm reg} \equiv \frac{1}{N_{\rm pix,reg}} \sum^{N_{\rm pix,reg}} I_\nu M_{\rm ptsrc}, \quad (2)$$

where $M_{\rm ptsrc}$ is a mask that is 1.0 for pixels in `SExtractor`-identified point sources and 0.0 otherwise. $N_{\rm pix,reg}$ refers to the total number of pixels in the region. Therefore, $\langle I_\nu^{\rm ptsrc}\rangle_{\rm reg}$ is the surface brightness of emission associated with point sources averaged over the entire control region.

From $\langle I_\nu^{\rm ptsrc}\rangle_{\rm reg}$, we estimate the fractional contribution of emission from point sources $f_{\rm ptsrc}$ to the overall emission in each field via

$$f_{\rm ptsrc} = \frac{N_{\rm pix,map}\langle I_\nu^{\rm ptsrc}\rangle_{\rm reg}}{\sum^{N_{\rm pix,map}} I_\nu}, \quad (3)$$

where the sum now goes over each whole map, with I_ν the surface brightness of each pixel and $N_{\rm pix,map}$ the number of pixels in the whole map.

Both the mean intensities and the fractional contributions of point sources to the flux are reported in Table 2. Averaged over large areas, the mean intensities of point sources are comparable to or less than the noise in the images (Table 1). Thus we expect them to have little impact on our analysis of the MIR color (Section 3.2) or comparison to CO (Section 3.4), where we focus on MIR intensities $\gtrsim$0.03 MJy sr^{-1}. They may affect our comparison to large-scale gas emission in Section 3.5.

The faint point sources contribute 1%–19% of the total MIR flux in the NGC 6822 fields and 24%–41% in WLM. The higher values in WLM reflect the fact that because of the faint, limited extended emission, point sources contribute fractionally more to WLM. The fact that $f_{\rm ptsrc}^{\rm F770W}$ is always larger than $f_{\rm ptsrc}^{\rm F2100W}$ reflects the higher sensitivity of F770W to emission from stars, which emit preferentially at shorter wavelengths.

3.2. F770W versus F2100W Emission

In the neutral ISM of solar-metallicity galaxies, the F770W filter captures mainly emission associated with the 7.7 μm PAH feature (e.g., J. D. T. Smith et al. 2007; C. M. Whitcomb et al. 2023b; R. Chown et al. 2025a). Meanwhile, continuum emission dominates the F2100W filter. In moderate radiation

[32] We assume that the surface density of such sources is roughly uniform across each field. This should be justified for any population of older stars, as the fields are small compared to the full size of each target (e.g., Figure 1). However, these calculations will not reflect the contribution of YSOs or other sources selectively associated with the star-forming complexes themselves.

Table 2
Contributions of Point Sources to Overall MIR Emission

Quantity	NGC 6822 #1	NGC 6822 #2	NGC 6822 #3	NGC 6822 #4	WLM
Mean intensity of hand-masked bright point sources $\langle I_\nu^{\rm ptsrc}\rangle_{\rm reg}$ ($\times 10^{-3}$ MJy sr^{-1})					
$\langle I_{\rm F770W}^{\rm ptsrc}\rangle_{\rm reg}$	10	44	8	20	5
$\langle I_{\rm F2100W}^{\rm ptsrc}\rangle_{\rm reg}$	5	22	10	5	5
Mean intensity of unmasked, fainter point sources $\langle I_\nu^{\rm ptsrc}\rangle_{\rm reg}$ ($\times 10^{-3}$ MJy sr^{-1})					
$\langle I_{\rm F770W}^{\rm ptsrc}\rangle_{\rm reg}$	37	46	18	41	30
$\langle I_{\rm F2100W}^{\rm ptsrc}\rangle_{\rm reg}$	7	51	35	44	77
Fractional contribution of fainter point sources to total flux in field (%)					
$f_{\rm ptsrc}^{\rm F770W}$	19	11	14	14	41
$f_{\rm ptsrc}^{\rm F2100W}$	1	2	6	3	24
Fraction of total MIR flux coming from CO-detected pixels (%)					
$f_{\rm CO\ det.}^{\rm F770W}$	39.9	15.4	68.4	8.5	40.9
$f_{\rm CO\ det.}^{\rm F2100W}$	56.4	19.2	85.5	7.4	72.2

Note. Fractional contributions of MIR point sources to the total emission in each JWST field $f_{\rm ptsrc}$ (Section 3.1) at native resolution, and fraction of the total MIR flux coming from CO-detected pixels $f_{\rm CO\ det.}$ at 2″ resolution. $\langle I_\nu^{\rm ptsrc}\rangle_{\rm reg}$ and $f_{\rm ptsrc}$ are defined in Equations (2) and (3), respectively. Pixels with surface brightness $\leqslant 0$ MJy sr^{-1} were excluded from the calculations.

fields, both bands capture stochastically heated emission (B. T. Draine & A. Li 2007). To first order, $I_\nu^{\rm F770W}/I_\nu^{\rm F2100W}$ and the similar ratio $I_\nu^{\rm IRAC\ 8\ \mu m}/I_\nu^{\rm MIPS\ 24\ \mu m}$ measured by Spitzer have often been taken to track the abundance of PAHs relative to larger grains (e.g., C. W. Engelbracht et al. 2005; K. D. Gordon et al. 2008; N. Li et al. 2020; J. Chastenet et al. 2023a; J. Sutter et al. 2024). We calculate $I_\nu^{\rm F770W}/I_\nu^{\rm F2100W}$ for all pixels detected at a signal-to-noise ratio SNR > 5.0 in both filters at 0.″9 resolution (2.0 and 4.3 pc for NGC 6822 and WLM, respectively) and plot the distribution of this ratio in Figure 5. This figure also shows results for the LMC, SMC, and PHANGS targets. Table 3 reports the median and scatter for each target.

Figure 5 shows a drop in the median $I_\nu^{\rm F770W}/I_\nu^{\rm F2100W}$ for metallicities below $Z = 0.4\,Z_\odot$; i.e., NGC 6822, WLM, and the SMC all show lower $I_\nu^{\rm F770W}/I_\nu^{\rm F2100W}$ or 8/24 μm compared to the LMC and the more massive PHANGS targets. Compared to the median PHANGS ratio $\log_{10}(I_\nu^{\rm F770W}/I_\nu^{\rm F2100W}) \approx 0.09$ or $I_\nu^{\rm F770W}/I_\nu^{\rm F2100W} \approx 1.23$, the NGC 6822 fields have on average a 0.58 dex lower ratio, with the most extreme fields, NGC 6822 Field 3 and WLM, reaching >0.8 dex, or >6×, lower.

This correlation between $I_\nu^{\rm F770W}/I_\nu^{\rm F2100W}$ and metallicity agrees with extensive work in the literature (e.g., A. Rémy-Ruyer et al. 2015; F. Galliano et al. 2018; N. Li et al. 2020; I. Shivaei & L. A. Boogaard 2024). Many Spitzer observations indicated low PAH abundances below metallicity of $12 + \log_{10}({\rm O/H}) \approx 8.2$, or $Z \approx 0.3\,Z_\odot$ (e.g., C. W. Engelbracht et al. 2005; J. M. Cannon et al. 2006; D. C. Jackson et al. 2006; B. T. Draine et al. 2007; K. D. Gordon et al. 2008), and the SMC ($0.2\,Z_\odot$) has lower PAH abundance than the LMC ($0.5\,Z_\odot$) (S. C. Russell & M. A. Dopita 1992; J. Chastenet et al. 2019). It remains an open question whether the PAH abundance steadily declines as a function of metallicity (e.g., F. Galliano et al. 2018), drops sharply at a specific Z (e.g., N. Li et al. 2020; C. M. Whitcomb et al. 2024), or depends on a third parameter such as specific star formation rate (A. Rémy-Ruyer et al. 2015). I. Shivaei & L. A. Boogaard (2024) found that for galaxies at intermediate redshift, the PAH fraction decreases sharply between $Z \approx 0.2$ and $0.3\,Z_\odot$.

Our observations demonstrate that the individual star-forming complexes at $Z = 0.2\,Z_\odot$ and $Z = 0.13\,Z_\odot$ show low but varied $I_\nu^{\rm F770W}/I_\nu^{\rm F2100W}$. We note that on their own these observations do not capture the transition from high to low metallicity, which would require a sample that better represents the metallicity distribution in the galaxy. We find significant scatter in the $I_\nu^{\rm F770W}/I_\nu^{\rm F2100W}$ ratios between fields, with a range of 0.56 dex, or a factor of 3.6, among the median $I_\nu^{\rm F770W}/I_\nu^{\rm F2100W}$ for different regions in NGC 6822. At lower resolution, e.g., the 50–100 pc typical of PHANGS observations, each region will be a single resolution element and this would manifest as point-to-point scatter.

We also see scatter in $I_\nu^{\rm F770W}/I_\nu^{\rm F2100W}$ within each region, and some of this appears to be physical in nature. The middle row in Figure 5 shows the map of $I_\nu^{\rm F770W}/I_\nu^{\rm F2100W}$ ratio for each field. These show regular patterns, including regions of depressed $I_\nu^{\rm F770W}/I_\nu^{\rm F2100W}$ (i.e., blue regions) within each field. These regions with low $I_\nu^{\rm F770W}/I_\nu^{\rm F2100W}$ correspond to the brightest Hα-emitting regions in our targets. To show this, we plot contours of Hα intensity in each field, with the level chosen by eye to correspond to the bright, compact Hα emission.[33] In all four NGC 6822 fields, the Hα-bright regions correspond to the regions in the map with low $I_\nu^{\rm F770W}/I_\nu^{\rm F2100W}$.

Table 3 and the bottom row of Figure 5 show $I_\nu^{\rm F770W}/I_\nu^{\rm F2100W}$ split into Hα-bright and Hα-faint regions. Across all metallicities, $I_\nu^{\rm F770W}/I_\nu^{\rm F2100W}$ drops inside H II regions. The drop from outside to inside H II regions is ≈0.50 dex for NGC 6822 as a whole, ≈0.32 dex for the SMC, and ≈0.23 dex for the LMC. A drop of ∼0.2 dex, similar in magnitude to our result, has been shown in the lower-

[33] A contour at 1×10^{-14} erg s^{-1} cm^{-2} arcsec^{-2} captures the bright, compact Hα emission in NGC 6822. Note that this contour is higher than the one used to separate the Magellanic Clouds into H II regions and neutral gas by J. Chastenet et al. (2019).

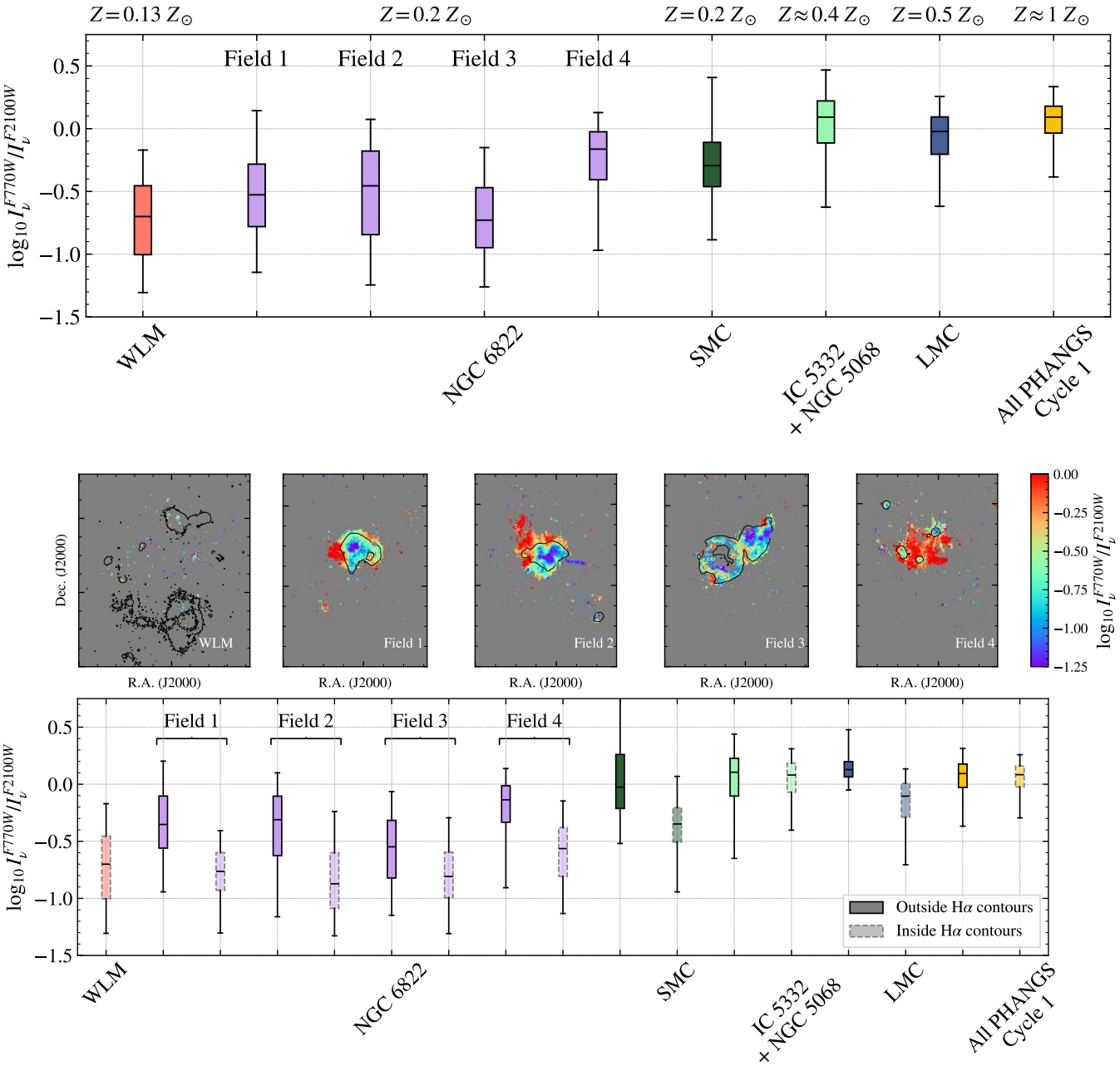

Figure 5. Top: box and whisker plots of $\log_{10}(I_\nu^{\rm F770W}/I_\nu^{\rm F2100W})$ for pixels with S/N > 5 in both filters for each target field and the comparison data set. The boxes show the 16th, 50th, and 84th percentiles, while the whiskers show the 5th and 95th percentiles. The NGC 6822 and WLM distributions are from 0.″9 resolution (2.0 and 4.3 pc, respectively) maps. We compare with the Magellanic Clouds (at $6'' \approx$ 1.5–2 pc resolution) and PHANGS Cycle 1 galaxies at ≈100 pc resolution, specifically highlighting the two dwarf galaxies in that sample, IC 5332 and NGC 5068. Metallicity increases from left to right (labeled at the very top of the figure). $I_\nu^{\rm F770W}/I_\nu^{\rm F2100W}$ drops below $Z \approx 0.2\ Z_\odot$ and NGC 6822 shows significant variations between fields. Middle: maps of $I_\nu^{\rm F770W}/I_\nu^{\rm F2100W}$ ratio for WLM and NGC 6822. The black contour shows an Hα intensity of 1×10^{-14} erg s^{-1} cm^{-2} arcsec^{-2}, which by eye corresponds to boundaries of bright, compact emission, and a reasonable proxy for the extent of the H II regions. These Hα-bright regions also correspond to depressions in $I_\nu^{\rm F770W}/I_\nu^{\rm F2100W}$ within the region. Bottom: like the top row, but now separating data sets into Hα-bright regions and other emission (WLM lacks enough faint emission to separate). The Hα-bright regions show lower $I_\nu^{\rm F770W}/I_\nu^{\rm F2100W}$ at all metallicities. Note that the distinction between inside and outside H II regions is coarse in PHANGS as the regions are not well resolved (Sections 2.5.1 and 3.2). The values for the top and bottom rows are provided in Table 3.

resolution PHANGS data by J. Sutter et al. (2024, and J. Chastenet et al. 2023b and O. V. Egorov et al. 2023) where each resolution element corresponds to a whole star-forming region (as noted in Section 2.5.1).

This result also agrees well with the literature. Reduced ratios of PAH to small dust grain intensity have also been found in infrared bubbles in the Milky Way (e.g., E. Churchwell et al. 2006; M. S. Povich et al. 2007) and the SMC (e.g., K. M. Sandstrom et al. 2010; Q.-L. Cui et al. 2024). Direct evidence for the suppression of PAH abundance within H II regions (compared to nearby well-shielded molecular regions) has been shown with JWST mid-IR spectroscopy of the Orion Bar photodissociation region (R. Chown et al. 2024b). Our measurements show that this suppression of $I_\nu^{\rm F770W}/I_\nu^{\rm F2100W}$ within the ionized gas of H II regions also occurs within each individual star-forming complex in NGC 6822. This lowers the ratio, which is already suppressed due to the low metallicity of the target, even further within H II regions.

Table 3
Median and Scatter of $\log_{10}$(F770W/F2100W)

		$\log_{10}$(Median F770W/F2100W) (dex)			
Name	$Z/Z_\odot$	Full Area	Outside Hα Cont.	Inside Hα Cont.	Inside/Outside
(1)	(2)	(3)	(4)	(5)	(6)
WLM	0.13	-0.70 ± 0.40	...	...	...
NGC 6822	0.20	-0.49 ± 0.47	-0.30 ± 0.35	-0.80 ± 0.30	-0.50 ± 0.47
Field 1	...	-0.53 ± 0.37	-0.35 ± 0.34	-0.76 ± 0.24	-0.41 ± 0.42
Field 2	...	-0.47 ± 0.48	-0.32 ± 0.36	-0.87 ± 0.35	-0.55 ± 0.51
Field 3	...	-0.73 ± 0.35	-0.55 ± 0.37	-0.81 ± 0.29	-0.25 ± 0.47
Field 4	...	-0.17 ± 0.25	-0.14 ± 0.22	-0.56 ± 0.30	-0.42 ± 0.37
SMC	0.20	-0.29 ± 0.26	-0.03 ± 0.32	-0.35 ± 0.22	-0.32 ± 0.39
PHANGS Dwarfs	0.40	0.06 ± 0.23	0.08 ± 0.22	0.08 ± 0.18	-0.00 ± 0.28
LMC	0.50	-0.02 ± 0.21	0.13 ± 0.10	-0.10 ± 0.20	-0.23 ± 0.22
PHANGS	1	0.09 ± 0.15	0.09 ± 0.14	0.08 ± 0.13	-0.01 ± 0.19

Note. The 0.″9 resolution JWST maps of NGC 6822 and WLM were used (2.0 and 4.3 pc, respectively). (3) All pixels included. (4) Including pixels outside the Hα contour $I(\mathrm{H}\alpha) = 1 \times 10^{-14}$ erg s^{-1} cm^{-2} arcsec^{-2} (to capture most of the Hα emission) and $I(\mathrm{H}\alpha) = 1.5 \times 10^{-15}$ erg s^{-1} cm^{-2} arcsec^{-2} for the Magellanic Clouds (from J. Chastenet et al. 2019). We split the PHANGS sample in a similar way using the catalog of H II regions (Section 2.5.1). (5) Including pixels within the Hα contour. (6) Ratio of column 5 to 4 (in $\log_{10}$ units).

In the Appendix we connect our $I_\nu^{\mathrm{F770W}}/I_\nu^{\mathrm{F2100W}}$ measurements to radiation field intensity, PAH abundance, and dust grain size distribution based on dust models. The overall reduced $I_\nu^{\mathrm{F770W}}/I_\nu^{\mathrm{F2100W}}$ seen in the dwarfs compared to PHANGS is qualitatively consistent with the reduced q_{PAH} that is expected at low Z. $I_\nu^{\mathrm{F770W}}/I_\nu^{\mathrm{F2100W}}$ depends nonlinearly on q_{PAH}, U, γ,[34] and dust size distribution, which we do not have constraints on, and so quantitatively ascribing the measured drop in $I_\nu^{\mathrm{F770W}}/I_\nu^{\mathrm{F2100W}}$ compared to PHANGS requires assumptions about these secondary parameters. We find that the values of $I_\nu^{\mathrm{F770W}}/I_\nu^{\mathrm{F2100W}}$ seen in the dwarfs imply reasonable values of q_{PAH} for a range of possible values of radiation field intensity and γ.

3.3. A Sublinear Power-law Scaling between 7.7 and 21 μm at High Intensity

Regions with suppressed $I_\nu^{\mathrm{F770W}}/I_\nu^{\mathrm{F2100W}}$ and bright Hα coincide with the highest MIR intensities observed in our fields. While $I_\nu^{\mathrm{F770W}}/I_\nu^{\mathrm{F2100W}}$ is suppressed in Hα-bright regions, these regions exhibit the highest absolute intensity values in our fields. Figure 6 illustrates this relationship through the median I_ν^{F770W} as a function of I_ν^{F2100W}, and Figure 7 demonstrates $I_\nu^{\mathrm{F770W}}/I_\nu^{\mathrm{F2100W}}$ as a function of I_ν^{F2100W}. The same 0.″9 resolution maps of I_ν^{F770W} and I_ν^{F2100W} of NGC 6822 and WLM from Section 3.2 were used. One can see from these figures that at high I_ν^{F2100W} (or high I_ν^{F770W}, not shown) the ratio $I_\nu^{\mathrm{F770W}}/I_\nu^{\mathrm{F2100W}}$ drops as a function of increasing MIR brightness, manifesting as a sublinear power-law relationship between I_ν^{F770W} and I_ν^{F2100W} at high intensities.

The SMC, LMC, PHANGS dwarfs, and NGC 6822 all show a common behavior in Figure 6. At low I_ν^{F2100W}, the targets show approximately fixed $I_\nu^{\mathrm{F770W}}/I_\nu^{\mathrm{F2100W}}$, leading to an approximately linear $I_\nu^{\mathrm{F770W}} - I_\nu^{\mathrm{F2100W}}$ relationship. Then above $I_\nu^{\mathrm{F2100W}} \approx 1$--$5$ MJy sr^{-1} they show declining $I_\nu^{\mathrm{F770W}}/I_\nu^{\mathrm{F2100W}}$ with increasing I_ν^{F2100W}. The entire PHANGS data set shows similar behavior, but with the turnover from a fixed to declining ratio (or linear to sublinear power law) at higher I_ν^{F2100W} (i.e., x_b in Equation (4)). We note that WLM does not show the same two-component behavior in our data, likely because we do not detect an extensive diffuse, fixed $I_\nu^{\mathrm{F770W}}/I_\nu^{\mathrm{F2100W}}$ component.

This behavior can be expressed as a two-part power law,

$$y = \begin{cases} a + b_1(x - x_b) & \text{for } x \leqslant x_b \\ a + b_2(x - x_b) & \text{for } x > x_b, \end{cases} \quad (4)$$

relating F770W intensity $y \equiv \log_{10} I_\nu^{\mathrm{F770W}}$ to $x \equiv \log_{10} I_\nu^{\mathrm{F2100W}}$. Because each of the binned relations in Figure 6 has a component at low intensity (around 1 MJy sr^{-1}) that is very close to a constant $I_\nu^{\mathrm{F770W}}/I_\nu^{\mathrm{F2100W}}$ ratio (i.e., a power-law slope of 1.0), we fix $b_1 = 1.0$; this also makes it easier to compare with Figure 5 and Table 3. We fit the binned data points with their uncertainties to Equation (4) using `scipy.curve_fit`. Table 4 reports broken power-law fits of this form for each target. Uncertainties in the best-fit parameters are given by the square root of the diagonal elements of the covariance matrix. Some regions are not well fit by a broken power law (with ⩽4 bins below x_b, making that part of the fit unreliable), and so for these regions we fit to a power law,

$$y = p + q(x - x_0), \quad (5)$$

where $x_0 \equiv \mathrm{median}(x)$.

Figure 7 resembles the relationship between R_{PAH} and Hα intensity (J. Chastenet et al. 2019; J. Sutter et al. 2024). This makes sense given the well-established correlation between I_ν^{F2100W} and Hα intensity (e.g., F. Belfiore et al. 2023). This, in turn, reflects the strong dust heating by UV radiation in and around H II regions and perhaps also the concentration of dust near H II regions. Then the break in the relationship and the onset of declining $I_\nu^{\mathrm{F770W}}/I_\nu^{\mathrm{F2100W}}$ corresponds to where H II regions dominate the emission along the line of sight, while the nearly fixed $I_\nu^{\mathrm{F770W}}/I_\nu^{\mathrm{F2100W}}$ at lower intensity corresponds to the neutral ISM. Then the vertical offsets among sources in Figure 6 just reflect the metallicity dependence of $I_\nu^{\mathrm{F770W}}/I_\nu^{\mathrm{F2100W}}$. The higher I_ν^{F2100W} turnover (x_b) where the

[34] γ is the fraction of dust mass exposed to radiation fields stronger than U_{min}. It represents the fraction of dust illuminated by a power-law distribution of radiation intensities between U_{min} and U_{max}.

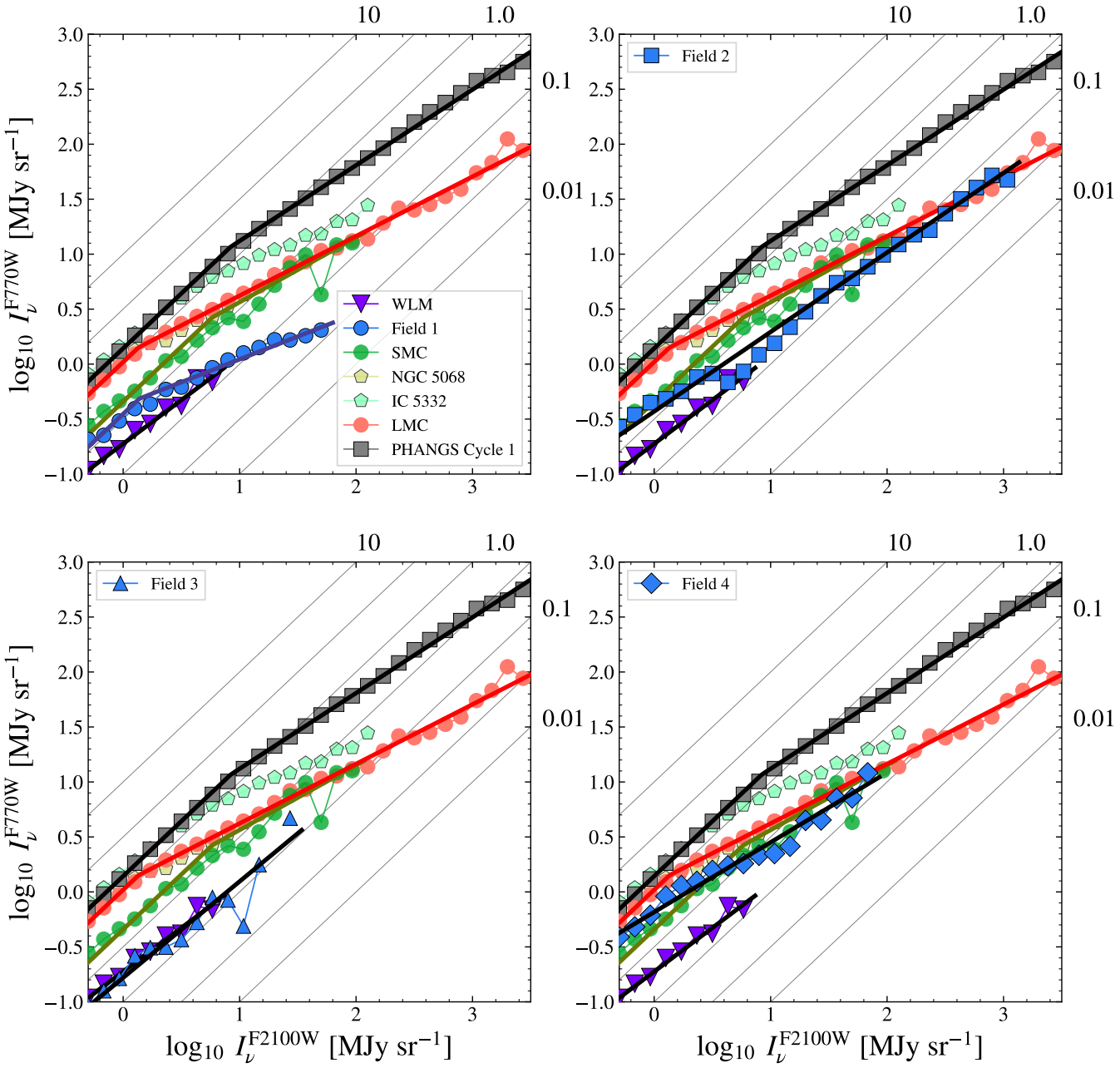

Figure 6. Binned measurements of I_ν^{F770W} vs. I_ν^{F2100W} in NGC 6822 and WLM at 0.″9 resolution (2.0 and 4.3 pc, respectively) compared to galaxies with a range of metallicities. Each of the four panels is the same except for the NGC 6822 field shown. For comparison we plot similar measurements for the LMC and SMC using Spitzer IRAC 8 μm and MIPS 24 μm on the x-axis at the MIPS 24 μm resolution ($\approx$2 pc); measurements from the full PHANGS Cycle 1 sample at coarser $\approx$100 pc resolution; and the specific PHANGS measurements for the dwarf galaxies NGC 5068 and IC 5332. Diagonal gray lines show constant $I_\nu^{F770W}/I_\nu^{F2100W}$. Fits, either single or broken power-law fits appear as solid lines (Section 3.3 and Table 4). The individual data sets show vertical offsets that can be attributed to metallicity (Section 3.2, Figure 7) but also a common shape, such that above $I_\nu^{F2100W} \approx 1$ MJy sr^{-1} (i.e., $x = 0$) all data sets show a sublinear power law, in which $I_\nu^{F770W}/I_\nu^{F2100W}$ declines with increasing I_ν^{F2100W}. This reflects the suppression of I_ν^{F770W} relative to I_ν^{F2100W} within H II regions due to PAH destruction in ionized gas.

$I_\nu^{F770W}/I_\nu^{F2100W}$–$I_\nu^{F2100W}$ anticorrelation begins in the main PHANGS sample likely reflects the higher dust column densities associated with the diffuse ISM in those more massive, dust-rich galaxies (e.g., D. Pathak et al. 2024).

3.4. MIR and CO(2–1) Emission

Figures 2 through 4 show bright MIR emission coincident with CO(2–1) emission detected by ALMA, and a main goal of our project is to use the MIR to trace otherwise hard-to-observe gas (Section 1) in these complexes. To that end, Figure 8 shows the relationships between I_ν^{F770W} and CO(2–1), and between I_ν^{F2100W} and CO(2–1), at 2″ resolution (Sections 2.1 and 2.2). The figure shows CO-detected pixels only, because unfortunately the lack of reliable short-spacing data precludes a stacking analysis in the ALMA data for these galaxies (e.g., see L. Neumann et al. 2023). The square symbols show the mean CO-to-MIR ratio for each of our target fields. Then Figure 9 shows these ratios as a function of metallicity for our target fields and comparison data. We quote

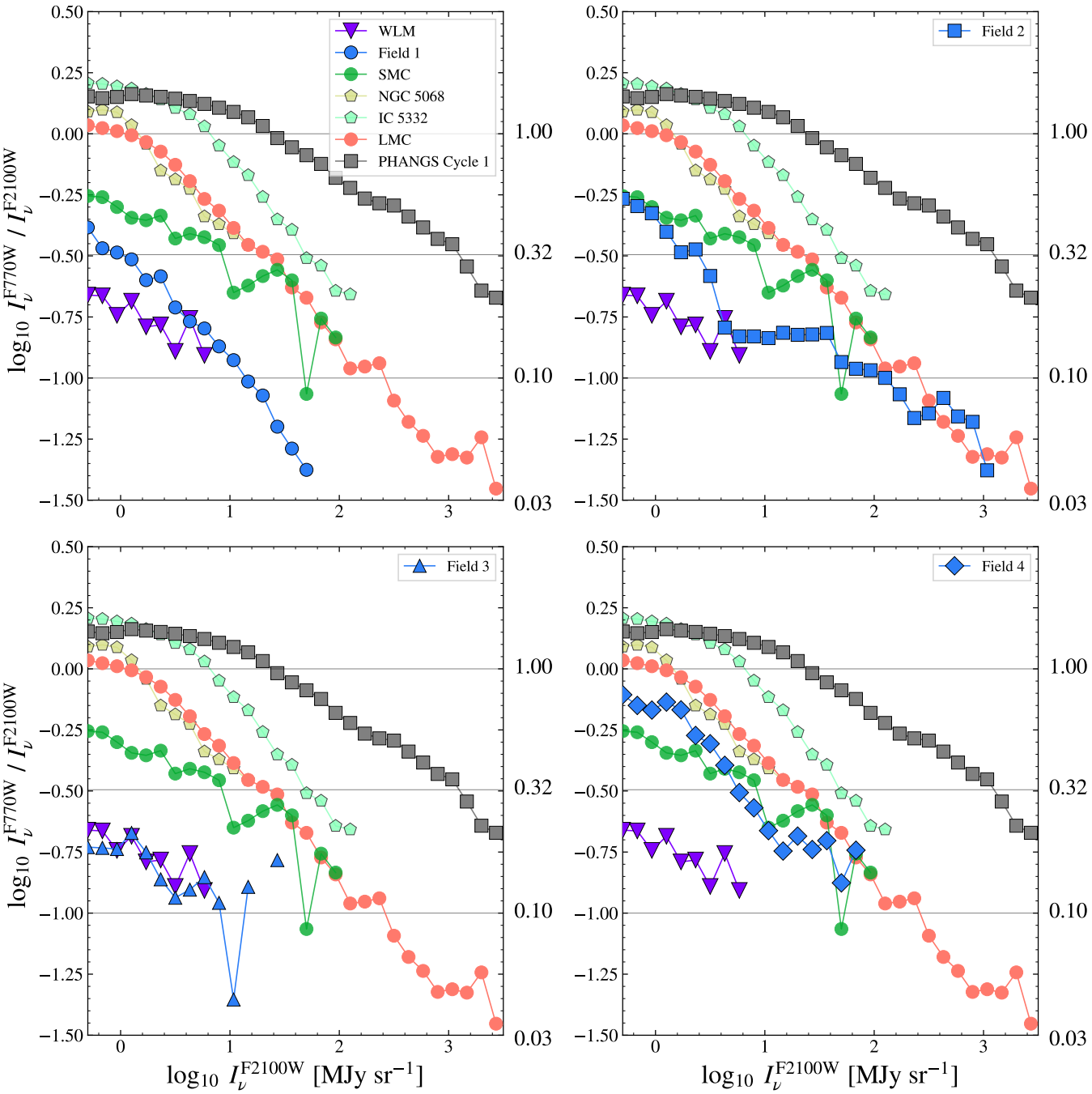

Figure 7. The same measurements from Figure 6 but with the y-axis expressed as a ratio. Horizontal lines indicate the constant ratios shown as diagonal lines in Figure 6. As in Figure 6 the data show vertical offsets that can be attributed to metallicity and a steady decline in $I_\nu^{F770W}/I_\nu^{F2100W}$ with increasing I_ν^{F2100W} at high I_ν^{F2100W}. This reflects the suppression of I_ν^{F770W} relative to I_ν^{F2100W} within H II regions due to PAH destruction in ionized gas.

the ratio of sums

$$\frac{\mathcal{R}_{CO/X}}{(\mathrm{K\ km\ s^{-1}})/(\mathrm{MJy\ sr^{-1}})} \equiv \left(\sum_{\mathrm{CO-det.}} \frac{I_{\mathrm{CO}(2-1)}}{\mathrm{K\ km\ s^{-1}}}\right) \times \left(\sum_{\mathrm{CO-det.}} \frac{I_\nu^X}{\mathrm{MJy\ sr^{-1}}}\right)^{-1}, \quad (6)$$

where X is the MIR band (either F770W or F2100W). The sum runs over the pixels with detected CO(2–1) emission, and we report the fraction of MIR emission associated with this selection in Table 2.

Figure 8 shows a large amount of scatter with many of the detected pixels from ALMA close to the noise limit in both galaxies. However, the mean CO-to-I_ν^{F770W} ratios for all four NGC 6822 fields and WLM resemble those found for the more massive galaxies by R. Chown et al. (2025a). In fact, as Figure 9 and Table 5 show, we observe similar CO-to-I_ν^{F770W} ratios for the whole PHANGS sample, the PHANGS dwarf subset, and the fields in NGC 6822. WLM shows a modest 0.44 dex depression with fainter CO relative to F770W ($\approx$3.4$\times$ below PHANGS). On the other hand, the right panels in Figures 8 and 9 show that the CO-to-I_ν^{F2100W} ratio does appear lower in our targets than in more massive galaxies, with

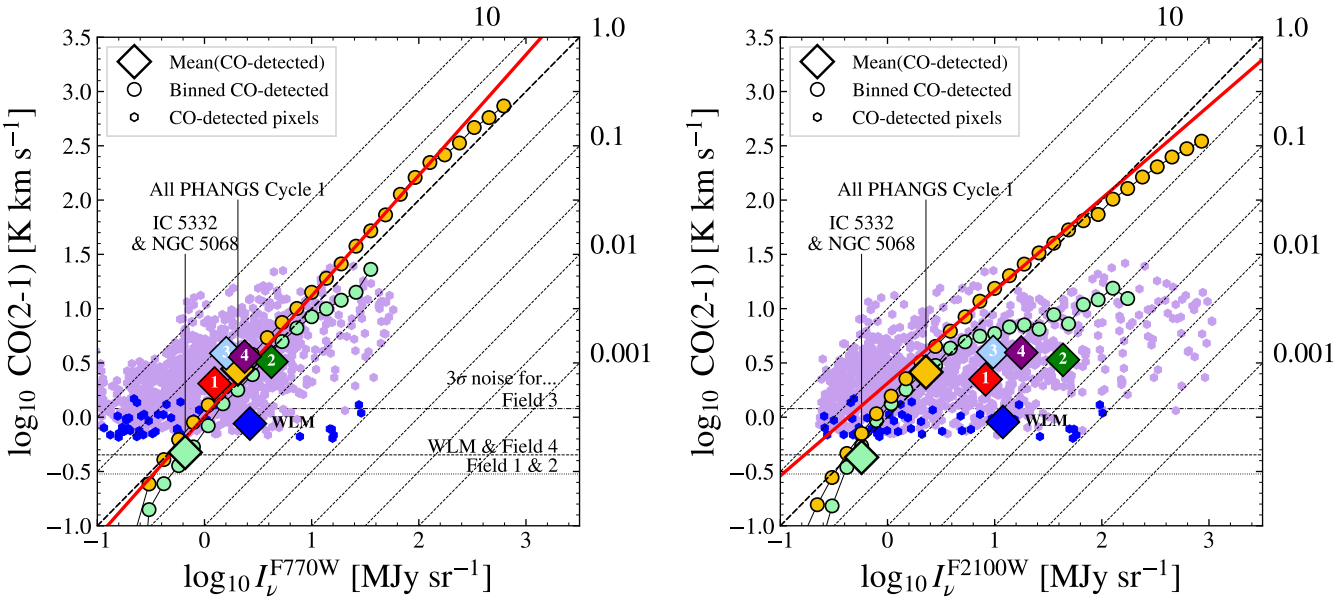

Figure 8. CO(2–1) intensity as a function of $I_\nu^{\rm F770W}$ (left) and $I_\nu^{\rm F2100W}$ (right) in NGC 6822 (small, purple symbols) and WLM (small, light red symbols) for CO-detected pixels (at $\geqslant 3\sigma$) at $2''$ resolution. Diagonal lines indicate constant CO(2–1)/MIR ratios. Horizontal lines indicate the 3σ CO noise levels for our data (Section 2.2). Diamond symbols show the average over CO-detected pixels for each sample. Fields 1–4 and WLM are labeled on or next to their diamond symbols. For comparison we show results for all PHANGS Cycle 1 galaxies (gold), and PHANGS dwarf galaxies (green). Solid lines show fits to these binned PHANGS data. While individual pixels and region-averages show some scatter, the CO to $I_\nu^{\rm F770W}$ ratio for detected regions in NGC 6822 and WLM resembles that seen for more massive and more distant PHANGS galaxies. In contrast, the CO to $I_\nu^{\rm F2100W}$ ratio appears lower in our targets than observed in the more massive PHANGS targets, with NGC 6822 and WLM showing ≈3–20× fainter CO emission at fixed F2100W surface brightness (Figure 9). CO/MIR ratios corresponding to the large diamonds are presented in Table 5.

Table 4
Best-fit Parameters of the F770W vs. F2100W Relationship Modeled as a Broken Power Law (Equation (4)) or a Single Power Law (Equation (5))

Name	$Z/ZZ_\odot$	x_0 ($\log_{10}$(MJy sr^{-1}))	x_b ($\log_{10}$(MJy sr^{-1}))	b_2	a ($\log_{10}$(MJy sr^{-1}))
WLM	0.13	0.167	⋯	0.796 ± 0.207	−0.592 ± 0.133
NGC 6822	0.20	1.300	⋯	0.741 ± 0.113	0.464 ± 0.129
Field 1	⋯	⋯	0.139 ± 0.550	0.416 ± 0.329	−0.314 ± 0.466
Field 2	⋯	1.300	⋯	0.723 ± 0.115	0.509 ± 0.130
Field 3	⋯	0.433	⋯	0.876 ± 0.249	−0.401 ± 0.190
Field 4	⋯	0.700	⋯	0.634 ± 0.147	0.261 ± 0.125
SMC	0.20	⋯	0.767 ± 0.457	0.589 ± 0.266	0.426 ± 0.431
IC 5332	0.37	⋯	0.407 ± 0.451	0.487 ± 0.296	0.593 ± 0.435
NGC 5068	0.38	0.367	⋯	0.606 ± 0.168	0.227 ± 0.123
LMC	0.50	⋯	0.135 ± 0.445	0.542 ± 0.178	0.154 ± 0.407
PHANGS	1.00	⋯	0.926 ± 0.478	0.688 ± 0.209	1.069 ± 0.467

Note. The $0\farcs9$ resolution JWST maps of NGC 6822 and WLM were used (2.0 and 4.3 pc, respectively). For the LMC and SMC, we replace F770W with IRAC 8 μm and F2100W with MIPS 24 μm. Fits were performed on binned measurements, incorporating uncertainties in x and y. For binned measurements, x uncertainties were set to half of the bin width. $\log_{10} x_0$ is the median of the x-values that go into the fit in the event that a single power law provides a better fit, and in these cases, the model is Equation (5). See Section 3.3 for details.

all four fields in NGC 6822 well below the CO-to-$I_\nu^{\rm F2100W}$ ratio measured for PHANGS targets, and WLM an order of magnitude lower (Tables 5 and 6). Overall, the CO/$I_\nu^{\rm F2100W}$ ratio appears to show some metallicity dependence, with the lowest values for WLM, then NGC 6822, then the PHANGS dwarfs, then the full PHANGS sample.

Our results show that as metallicity decreases, CO and PAH emission decrease by similar amounts, at least within CO-detected areas of each complex. The result is a surprisingly stable CO-to-$I_\nu^{\rm F770W}$ ratio. Meanwhile the drop in CO-to-$I_\nu^{\rm F2100W}$ may indicate that the CO molecule (like the PAHs producing $I_\nu^{\rm F770W}$) is more fragile and sensitive to metallicity than the grains that produce the $I_\nu^{\rm F2100W}$. In that sense, the CO-to-$I_\nu^{\rm F2100W}$ ratio may reflect the CO-to-dust ratio, which has often been observed to be lower in low-metallicity dwarf galaxies and used as a way to infer the CO-to-H_2 conversion factor (e.g., A. K. Leroy et al. 2011; Y. Shi et al. 2015; I.-D. Chiang et al. 2024).

The fields in NGC 6822 do not show identical results. Fields 2 and 4 show the highest fraction of MIR emission coincident with CO and also the lowest CO-to-MIR ratios in both bands. These are also the two fields with the most extensive CO detections and the highest $I_\nu^{\rm F770W}/I_\nu^{\rm F2100W}$ ratios. As discussed by A. Schruba et al. (2017) these complexes are in distinct evolutionary stages. Our measurements show Fields 2 and 4 in a phase with more abundant CO emission, abundant PAHs relative to small dust, and spatially concentrated bright MIR emission.

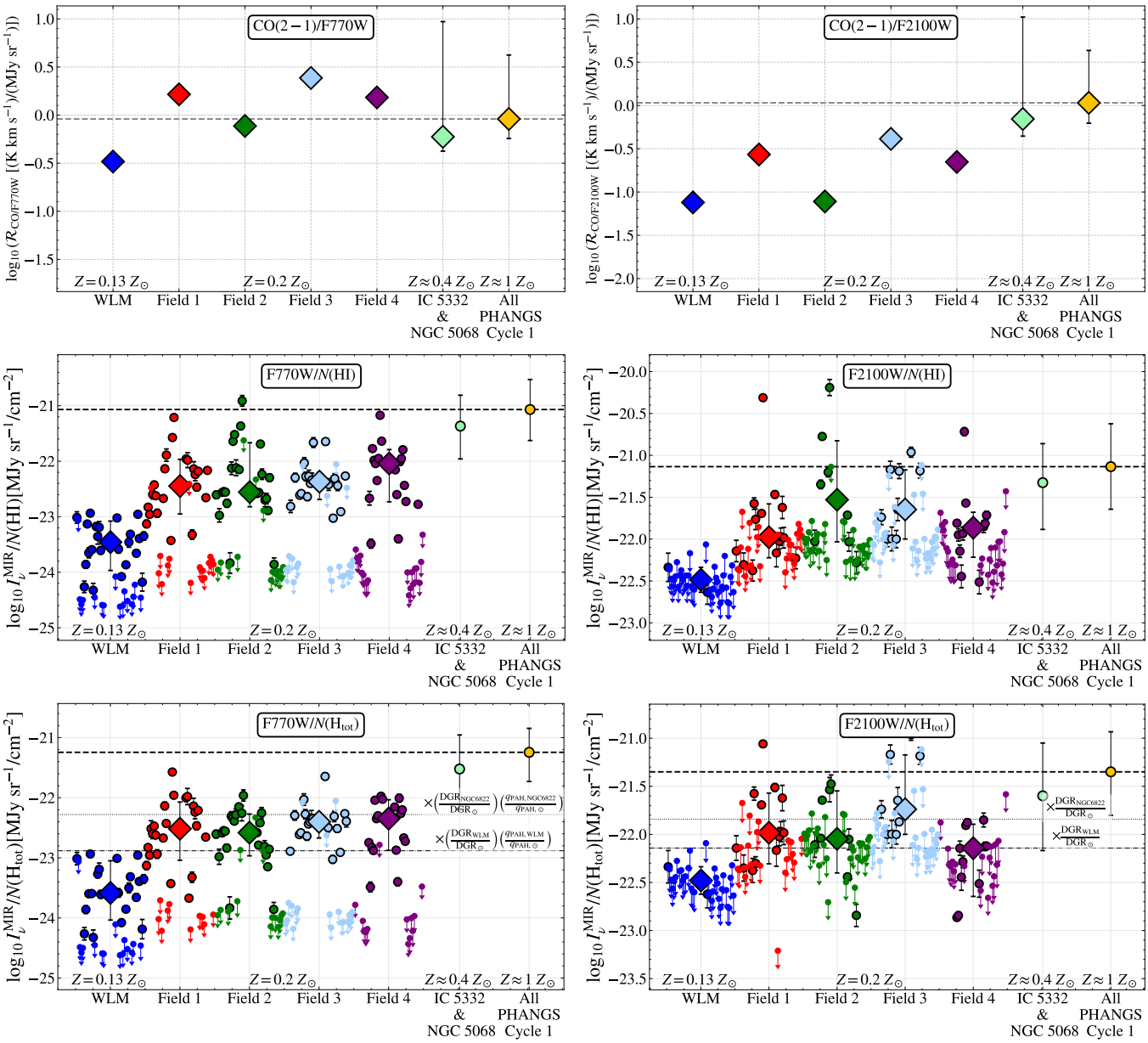

Figure 9. Ratios of MIR emission to gas tracers. Top row: average $I_{\mathrm{CO(2-1)}}$ divided by average I_ν^{F770W} (left) and I_ν^{F2100W} (right; Equation (6)). The horizontal line indicates the median CO/MIR intensity ratio for PHANGS. The error bars show 16th–84th percentiles. The averages were calculated from CO and MIR maps at 2″ resolution, and only including pixels where CO emission is detected and the MIR intensity has SNR > 5. Metallicity increases from left to right (but not to scale). NGC 6822 and WLM exhibit $\mathrm{CO}/I_\nu^{\mathrm{F770W}}$ ratios similar to those in PHANGS, while their $\mathrm{CO}/I_\nu^{\mathrm{F2100W}}$ ratios are lower by 0.5–1.5 dex. The second and third rows show $I_\nu^{\mathrm{MIR}}/N(\mathrm{HI})$ and $I_\nu^{\mathrm{MIR}}/N(\mathrm{H_{tot}})$, calculated in circular apertures of 10″ radius that cover the fields (Figure 10). The diamonds and error bars indicate the median and 16th–84th percentiles for apertures with detected MIR emission. WLM and NGC 6822 both show suppressed $I_\nu^{\mathrm{MIR}}/N(\mathrm{HI})$ and $I_\nu^{\mathrm{MIR}}/N(\mathrm{H_{tot}})$ compared to PHANGS. The dashed lines in the bottom panels show the expected ratios accounting for the lower dust-to-gas ratio and PAH abundance in our targets. These lower abundances appear to explain the typical $I_\nu^{\mathrm{MIR}}/N(\mathrm{H_{tot}})$ detected regions of NGC 6822, but upper limits and measurements for WLM suggest additional suppression of PAH and dust emission from the diffuse ISM. For the corresponding scatter plots see Figures 8 (top row) and 12 (middle and bottom rows). The per-field medians are shown in Table 5, and compared to PHANGS in Table 6.

A region in the southern part of Field 4 is an interesting exception to the overall correlation between CO and I_ν^{F770W}. There, we find a region with detected CO and I_ν^{F770W}, and a high CO/F770W ratio of about 20.

3.5. MIR Emission, Atomic Gas, and Total Neutral Gas

Finally, we compare F770W and F2100W emission to atomic and total gas column density. A high column density of H I is present over the whole area of all of our fields and represents the majority of the total gas along most lines of sight. Based on B. T. Draine et al. (2007), M. Compiègne et al. (2008), and B. T. Draine (2011), to first order we expect

$$I_\nu^{\mathrm{F770W}}/N(\mathrm{H_{tot}}) \propto \mathrm{DGR} \times U \times q_{\mathrm{PAH}}, \quad (7)$$

and

$$I_\nu^{\mathrm{F2100W}}/N(\mathrm{H_{tot}}) \propto \mathrm{DGR} \times U, \quad (8)$$

with U the intensity of the interstellar radiation field, DGR the dust-to-gas ratio, q_{PAH} the PAH abundance, and $N(\mathrm{H_{tot}})$ the

Table 5
CO(2–1)-to-MIR Ratios, MIR-to-H I, and MIR-to-$N(H_{tot})$ in NGC 6822 and WLM, Compared to PHANGS

Target(s) (1)	CO(2–1)/F770W (2)	CO(2–1)/F2100W (3)	F770W/N(H I) (4)	F2100W/N(H I) (5)	F770W/$N(H_{tot})$ (6)	F2100W/$N(H_{tot})$ (7)
PHANGS		$0.03^{+0.61}_{-0.23}$	$-21.07^{+0.54}_{-0.56}$	$-21.13^{+0.51}_{-0.51}$	$-21.24^{+0.40}_{-0.49}$	$-21.35^{+0.42}_{-0.45}$
IC 5332 and NGC 5068	$-0.23^{+1.20}_{-0.15}$	$-0.16^{+1.18}_{-0.20}$	$-21.37^{+0.56}_{-0.59}$	$-21.33^{+0.47}_{-0.56}$	$-21.52^{+0.57}_{-0.67}$	$-21.60^{+0.55}_{-0.57}$
NGC 6822	$0.17^{+0.01}_{-0.01}$	$-0.68^{+0.01}_{-0.01}$	$-22.35^{+0.35}_{-0.35}$	$-21.75^{+0.30}_{-0.30}$	$-22.46^{+0.27}_{-0.27}$	$-21.98^{+0.29}_{-0.29}$
Field 1	$0.22^{+0.01}_{-0.01}$	$-0.57^{+0.01}_{-0.01}$	$-22.45^{+0.48}_{-0.50}$	$-21.98^{+0.40}_{-0.25}$	$-22.52^{+0.44}_{-0.52}$	$-21.98^{+0.41}_{-0.32}$
Field 2	$-0.113^{+0.004}_{-0.004}$	$-1.109^{+0.004}_{-0.004}$	$-22.56^{+0.89}_{-0.26}$	$-21.53^{+0.70}_{-0.50}$	$-22.58^{+0.31}_{-0.38}$	$-22.05^{+0.50}_{-0.35}$
Field 3	$0.39^{+0.04}_{-0.04}$	$-0.39^{+0.04}_{-0.04}$	$-22.37^{+0.17}_{-0.32}$	$-21.65^{+0.47}_{-0.35}$	$-22.40^{+0.13}_{-0.27}$	$-21.74^{+0.57}_{-0.26}$
Field 4	$0.184^{+0.006}_{-0.006}$	$-0.652^{+0.006}_{-0.006}$	$-22.04^{+0.25}_{-0.69}$	$-21.86^{+0.18}_{-0.35}$	$-22.35^{+0.31}_{-0.53}$	$-22.14^{+0.25}_{-0.50}$
WLM	$-0.48^{+0.04}_{-0.04}$	$-1.12^{+0.05}_{-0.05}$	$-23.46^{+0.38}_{-0.51}$	$-22.49^{+0.15}_{-0.15}$	$-23.58^{+0.53}_{-0.45}$	$-22.48^{+0.14}_{-0.14}$

Notes. All quantities are expressed in $\log_{10}$ units, and uncertainties are 16th–84th percentiles. Columns (2) and (3) are $\log_{10}(I_{CO(2-1)}/I_\nu^{MIR})$ ratios in units of K km s^{-1}/(MJy sr^{-1}), as defined in Equation (6). Columns (4)–(7) are $\log_{10}(I_\nu^{MIR}/N(H_{tot}))$ ratios in units of MJy sr^{-1}/cm^{-2}. Columns (2) and (3) are plotted in the first row of Figure 9, while columns (4)–(7) are shown in the second and third rows of that figure. See Sections 3.4 and 3.5 for details.
[a] The entry for CO/F770W (column (2)) can be compared with the value of $\log_{10}$(CO(2–1)/F770W) (not starlight-subtracted) from Table 2, row (3) of R. Chown et al. (2025a), which is 0.00 ± 0.35 dex. The (statistically insignificant) difference in the median ratio is because of the different samples employed: we use the 19 PHANGS Cycle 1 Treasury targets while that analysis used 70 targets (Cycles 1 + 2).

Table 6
$\log_{10}(I_\nu^{MIR}/N(H_{tot}))$ Ratios for F770W and F2100W, Normalized by Their Respective Ratios Measured from PHANGS Galaxies (Row (1) of Table 5), with Dust-to-Gas Ratio and PAH Abundances Normalized to PHANGS Values for Comparison

Target(s) (1)	$\Delta\log_{10}\frac{I_\nu^{F770W}}{N(H_{tot})}$ (2)	$\Delta\log_{10}$DGR q_{PAH} (3)	$\Delta\log_{10}\frac{I_\nu^{F2100W}}{N(H_{tot})}$ (4)	$\Delta\log_{10}$DGR (5)
NGC 6822	$-1.22^{+0.43}_{-0.53}$	−1.04	$-0.63^{+0.47}_{-0.49}$	−0.49
Field 1	$-1.27^{+0.60}_{-0.71}$	…	$-0.63^{+0.59}_{-0.56}$	…
Field 2	$-1.34^{+0.51}_{-0.62}$	…	$-0.70^{+0.65}_{-0.58}$	…
Field 3	$-1.16^{+0.42}_{-0.55}$	…	$-0.39^{+0.70}_{-0.52}$	…
Field 4	$-1.10^{+0.51}_{-0.72}$	…	$-0.79^{+0.49}_{-0.68}$	…
WLM	$-2.34^{+0.67}_{-0.66}$	−1.64	$-1.13^{+0.44}_{-0.47}$	−0.79

Note. Columns (2) and (4) show columns (5) and (7) of Table 5 divided by the first row of that table. The values here are the large diamonds in the bottom row of Figure 9 divided by the value of the black dashed line. The first row is the mean of Fields 1–4 in NGC 6822. Guided by Equations (7) and (8), column (3) (to be compared with column (2)) shows the product of dust-to-gas ratio (DGR) and PAH abundance q_{PAH} divided by their PHANGS values (see note in Table 1 for how DGR was estimated), and column (5) (to be compared with column (4)) shows the same but with just DGR. Since we do not constrain DGR or q_{PAH} here, we use galaxy-integrated values. This is illustrated in the bottom row of Figure 9. See Section 3.5 for details.

total gas column density,

$$N(H_{tot}) \equiv N(H\,I) + 2N(H_2). \quad (9)$$

Here we use the 2″ resolution MIR and CO maps, and the ≈8″ resolution H I maps. We place circular apertures of 10″ radius that span each field (Figures 10 and 11). This aperture size was chosen to encompass the FWHM ≈8″ beam of our H I maps. Within each aperture, we measure the median I_ν^{F770W}, median I_ν^{F2100W}, H I column density (N(H I)), and total H column density (Equation (9)), assuming the CO-to-H_2 conversion factors in Section 2.2. We use the median when calculating these aperture-averaged intensities in order to suppress the contribution of MIR point sources (Section 3.1).

The second and third rows of Figure 9 show the MIR-to-N(H I) and MIR-to-$N(H_{tot})$ ratios for each aperture, and Figure 12 compares MIR intensity and gas column density via scatter plots. In NGC 6822, I_ν^{F770W}-detected apertures show $I_\nu^{F770W}/N(H_{tot})$ well below those in PHANGS galaxies. Apertures with detected MIR emission in WLM show even lower $I_\nu^{F770W}/N(H_{tot})$ ratios than NGC 6822. The right panels show a similar situation for $I_\nu^{F2100W}/N(H_{tot})$, with the median ratios of detected apertures lower in NGC 6822 than in PHANGS, and again even lower in WLM than in NGC 6822. Each of our fields also shows a significant number of apertures with only an upper limit for I_ν^{F770W}, and these limits imply even lower $I_\nu^{F770W}/N(H_{tot})$ than we measure for detected apertures. Upper limits are even more common for I_ν^{F2100W} than I_ν^{F770W}, reflecting the higher noise in the F2100W data, so this ratio shows even more upper limits. These measurements match the visual impression that atomic gas covers the whole field, while extended PAH and dust emission are fainter and patchier.

Figure 12 shows the same measurements via scatter plots of I_ν^{F770W} and I_ν^{F2100W} as a function of N(H I) and $N(H_{tot})$. Compared to PHANGS measurements for H II regions (grayscale), both of our targets show similar high column densities, but significantly lower I_ν^{F770W} and moderately lower I_ν^{F2100W} at fixed column density compared to PHANGS. Despite higher column densities WLM shows even lower intensity in both bands than NGC 6822. The figure again highlights the large number of apertures with upper limits. It also shows how the apertures with relatively high $I_\nu^{F770W}/N(H_{tot})$ or $I_\nu^{F2100W}/N(H_{tot})$ are also those with high $N(H_{tot})$. These tend to be the peaks of the complexes, which also harbor the detected CO emission.

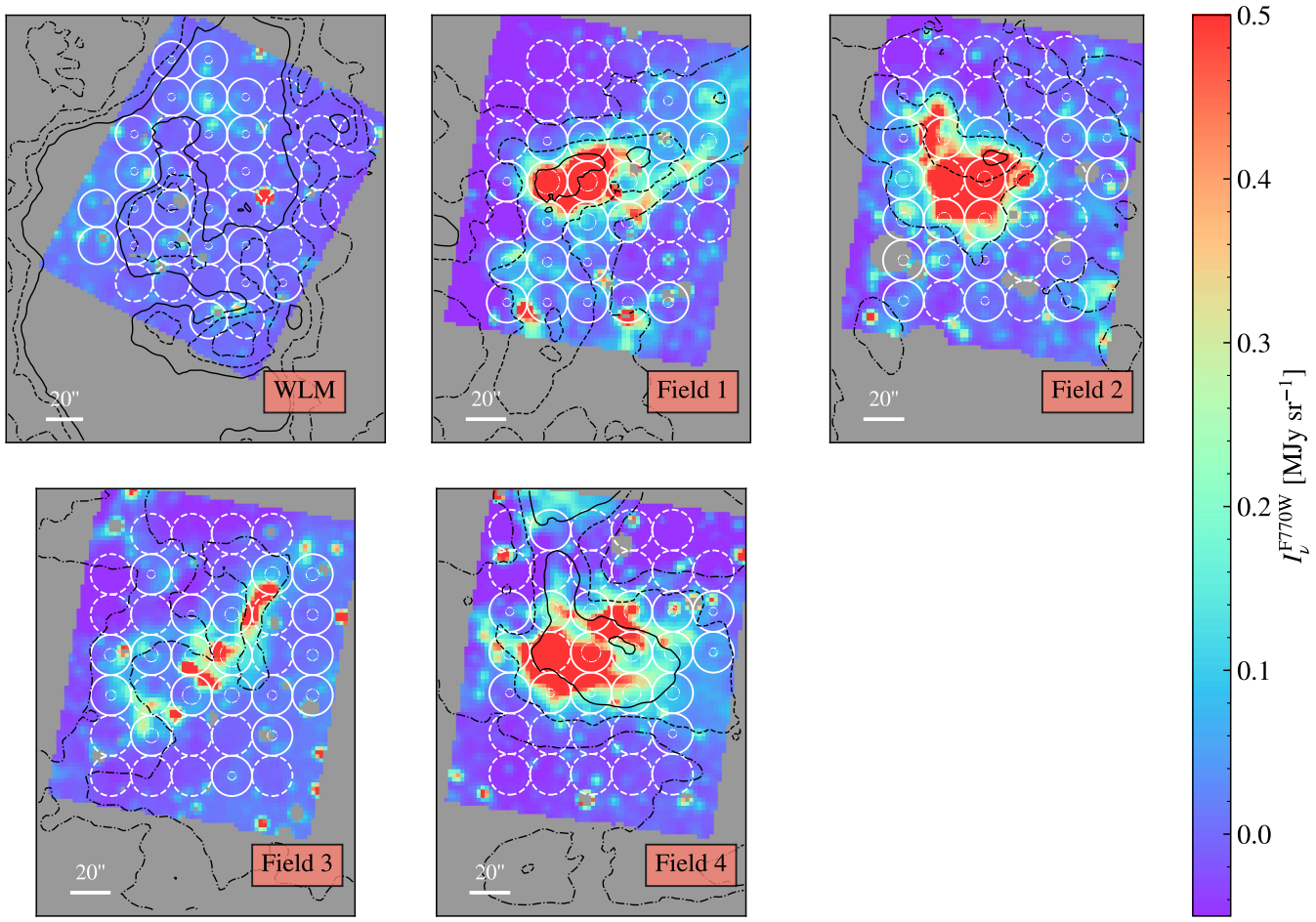

Figure 10. JWST F770W (top) and F2100W (bottom) images of WLM and NGC 6822 Fields 1–4 with H I column density contours of 10^{21} cm^{-2} (dotted–dashed), 1.7×10^{21} cm^{-2} (dashed), and 2.2×10^{21} cm^{-2} (thick solid). The circular apertures (10″ radius) were selected such that they sample variations in mid-IR and H I inside and outside the H II regions (see Section 3.5). Each 10″ aperture contains additional information about the $I_\nu^{\rm F770W}/N({\rm H_{tot}})$ ratio in that aperture. If the ratio is undetected (upper limits in Figure 12), the aperture has a dashed boundary, otherwise it has a solid boundary. Detected apertures have an inner circular aperture indicating the value of the measured $I_\nu^{\rm F770W}/N({\rm H_{tot}})$ ratio, with a radius of 10″ corresponding to $\log_{10}(I_\nu^{\rm F770W}/N({\rm H_{tot}})) = -20.5$, and a radius of 1″ corresponding to −23. One can see that the largest ratios are found in the brightest parts of the complexes. Interestingly, the middle of the bubble of Field 3 shows a nondetection in the ratio, and is suppressed in both gas content and PAH emission. The average properties of these apertures are shown in Figure 12. A version of this plot with F2100W instead of F770W is shown in Figure 11.

The measurements in Figure 12 are shown in Table 5, and again in Table 6 but normalized to the PHANGS values, next to estimates of the fractional change in the ratios expected given changes in DGR and $q_{\rm PAH}$ (Equations (7) and (8)). The colored dashed lines in the bottom panels of Figure 9 show the fiducial expectations in Table 6.

In NGC 6822, the median $\log_{10}(I_\nu^{\rm F770W}/N({\rm H_{tot}}))$ and $\log_{10}(I_\nu^{\rm F2100W}/N({\rm H_{tot}}))$ for detected apertures appear overall consistent with the fiducial expectation. WLM shows lower ratios, consistent with the true DGR or $q_{\rm PAH}$ in the diffuse ISM of WLM being even lower than our adopted values. As we remark above, the WLM MIR images appear largely devoid of extended emission even though these observations are deeper than those for NGC 6822 and the H I column densities are higher in this target. WLM's high inclination may also play a role here, as high inclination leads to high H I column densities, but will also lead to the inclusion of gas from the extended H I reservoir in each measurement, including the outskirts of the galaxy.

Both fields show many (3σ) upper limits. For F770W, the majority of the upper limits indicate $\log_{10}(I_\nu^{\rm F770W}/N({\rm H_{tot}}))$ significantly below the measured detections. As noted in Section 2.1, our tests show that the background level of the JWST observations is uncertain at the $\approx$0.1 MJy sr^{-1} level. Our quoted upper limits, which are derived from estimates of the instrumental noise, do not account for this term. Figure 12 shows that even in the extreme case where we considered all intensities below 0.1 MJy sr^{-1} ($\log_{10} I_\nu = 0.1$) as upper limits, both targets would lie well below the PHANGS targets in both bands.

Figure 10 shows $I_\nu^{\rm F770W}/N({\rm H_{tot}})$ for individual apertures. Detections are shown as solid circles, while nondetections have dashed boundaries and no inner apertures. Inside each detected aperture, the size of the second, inner circle is proportional to $\log_{10}(I_\nu^{\rm F770W}/N({\rm H_{tot}}))$. The largest ratios follow the bright MIR emission, while the outskirts of each field show many nondetections. The figure shows that fainter, extended F770W emission follows the distribution of H I emission in each complex. The center of the bubble in Field 3 provides a striking example of this correlation, showing depressed H I emission, faint or undetected F770W, and a lower $I_\nu^{\rm F770W}/N({\rm H_{tot}})$ ratio than the apertures around the border of the bubble. In addition to the destruction of PAHs within the ionized gas in the center of the bubble, this shows pileups of

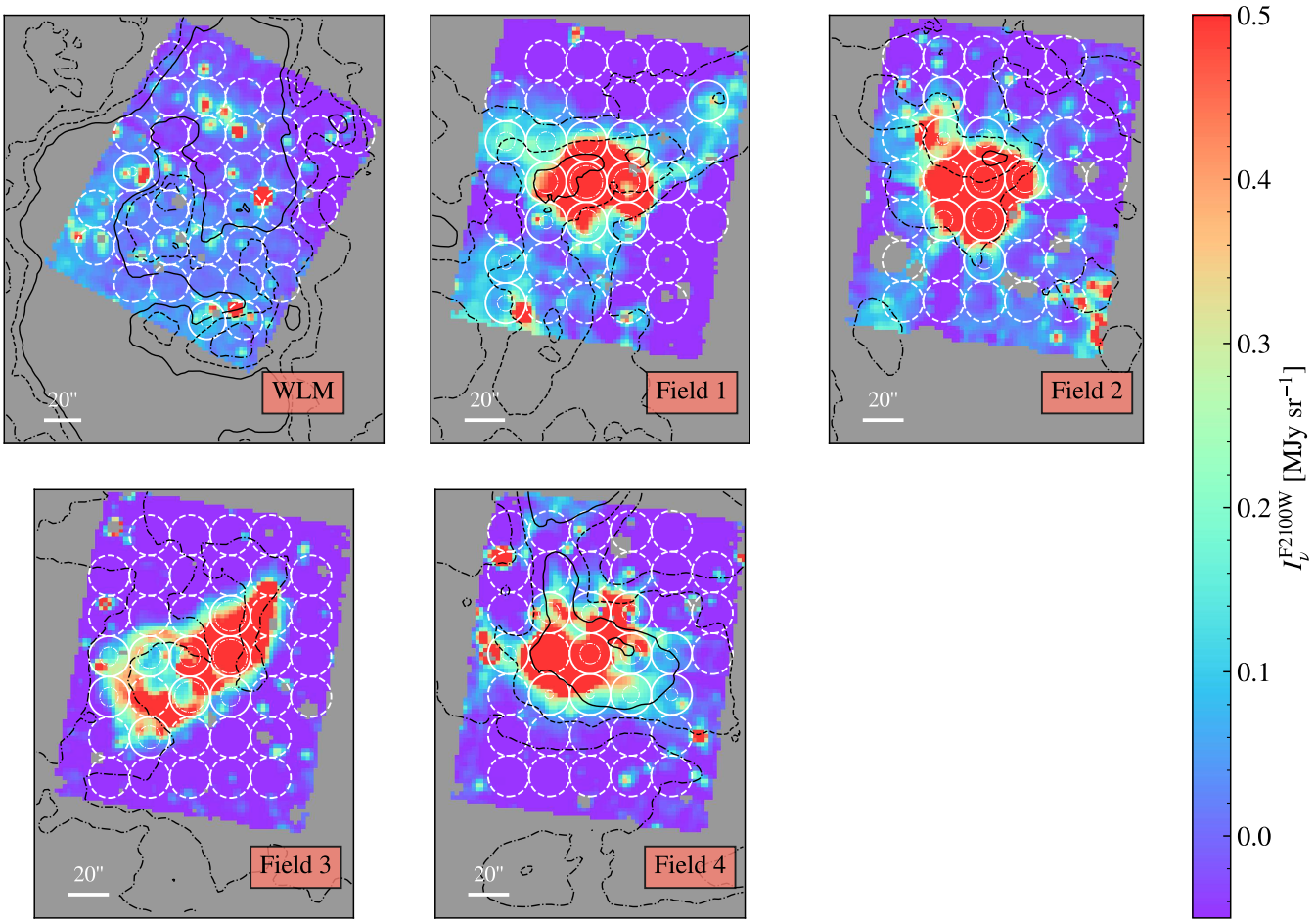

Figure 11. As in Figure 10 but with F2100W instead of F770W.

both gas and dust at the edges of the expanding bubble. The version of this plot with F2100W in place of F770W is shown in Figure 11.

Finally, we note that U, the intensity of the interstellar radiation field, appears in Equations (7) and (8). All other things being equal, MIR emission should be brighter in regions with more intense radiation. We currently lack resolved estimates of U within our regions, but note that it should be high near the massive O and B stars powering the regions. We note that the diffuse interstellar radiation field in the SMC appears consistent with or higher than the intensity of the solar neighborhood field (J. Chastenet et al. 2019; D. Utomo et al. 2019), so there is no evidence that dust or PAH emission will "hide" due to low U fields in these environments.

4. Conclusions

With the goal of constraining the evolution of small dust grains at low metallicity and exploring the utility of PAH and small dust grain emission to trace cold gas, we have used JWST/MIRI to image mid-infrared emission from two of the closest star-forming, low-metallicity dwarf galaxies, NGC 6822 ($Z = 0.2\,Z_\odot$, $D = 474$ kpc) and WLM ($Z = 0.13\,Z_\odot$, $D = 985$ kpc). We present new 0.7–3.3 pc resolution F770W and F2100W images that cover the main star-forming regions in each galaxy (four regions in NGC 6822 and one in WLM). In more massive galaxies, F770W observations are dominated by the 7.7 μm PAH band, while the F2100W filter is dominated by emission from stochastically heated small dust grains at $\approx$21 μm.

The MIR images of NGC 6822 (Figures 2 and 3) reveal bright emission with detailed structure. We observe filaments, edge-brightened bubbles, extended diffuse emission, and a plethora of point sources of various types. The MIR emission in NGC 6822 appears bright with extended structure, but is still confined relative to the diffuse atomic gas (visible from new LGLBS VLA observations: N. M. Pingel et al. 2024, E. Koch et al. 2025, in preparation). This atomic gas extends at high column densities across each field and far beyond (Figure 1), while the MIR emission appears mostly confined to the fields covered by our observations. In contrast to NGC 6822, MIR emission from the lower-metallicity galaxy WLM (Figure 4) shows barely any extended emission, with dust emission mostly limited to a smaller number of point sources.

We compare these images to one another, to maps of CO and 21 cm emission tracing the cold gas, to Spitzer observations of the Magellanic Clouds, and to PHANGS-JWST observations of more massive galaxies, and find:

1. Employing $I_\nu^{\rm F770W}/I_\nu^{\rm F2100W}$ as an empirical tracer of the PAH abundance (see Appendix), we find that NGC 6822 and WLM both show suppressed PAH abundance compared to more massive, nearly solar-metallicity galaxies in PHANGS-JWST (Figures 5 and 6, Tables 3 and 4). We

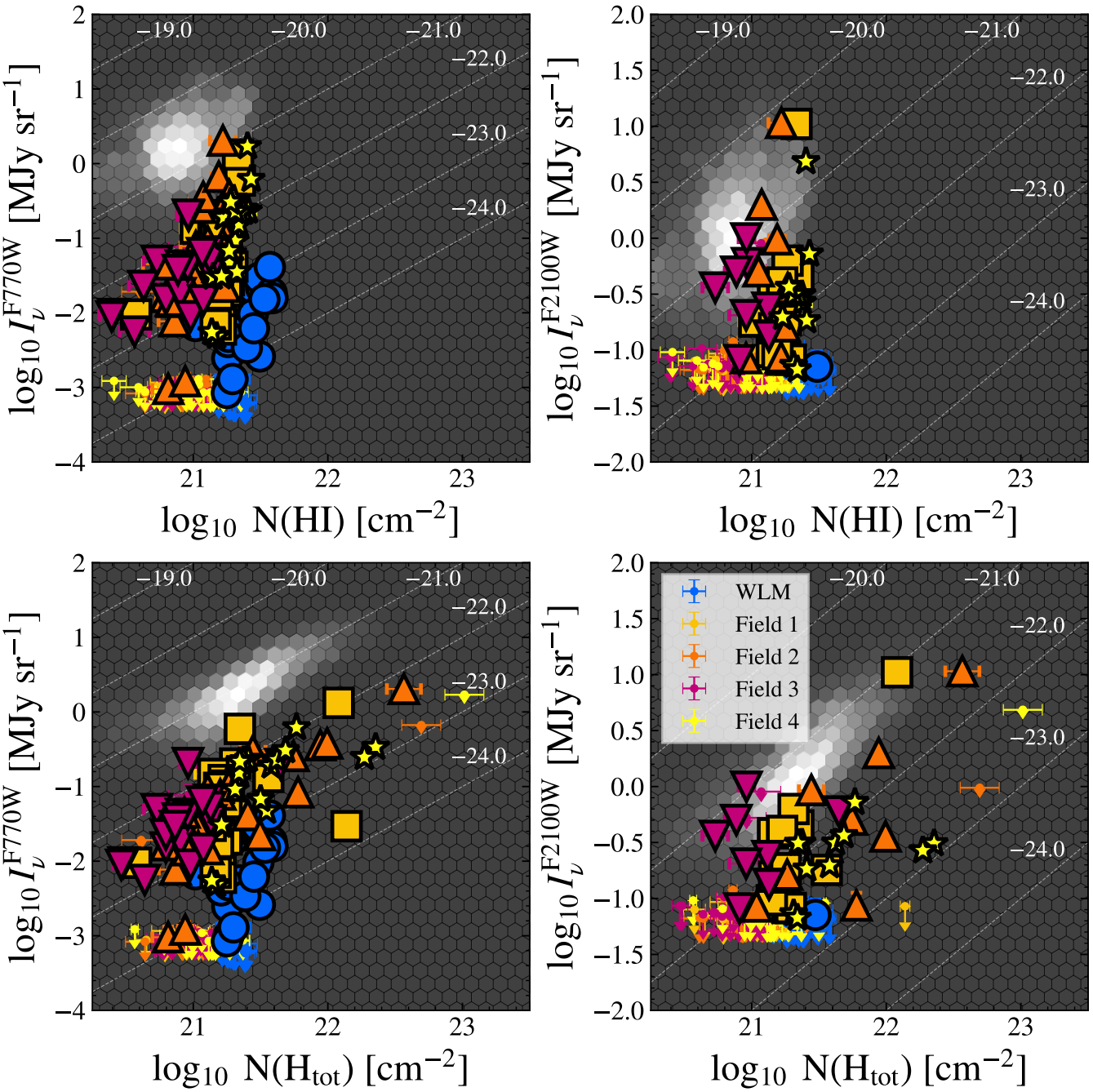

Figure 12. Relationships between average mid-IR emission and H I column density (top row), and total H column density (bottom row) assuming appropriate α_{CO} (Section 2.2). Vertical error bars are the measurement uncertainty, while horizontal error bars indicate scatter. Data points are for apertures on the images, selected by eye to capture variations in relative MIR, H I, and CO surface brightnesses (Section 3.5). Diagonal lines show constant values of $\log_{10}(I_\nu^{MIR}/N(\mathrm{H\,I}))$ (top) or $\log_{10}(I_\nu^{MIR}/N(\mathrm{H_{tot}}))$ (bottom) ratios (in units of $\log_{10}(\mathrm{MJy\ sr^{-1}})/\mathrm{cm^{-2}}$). Detections are indicated as filled symbols with black borders, while 3σ upper limits of nondetections are smaller circles with arrows. The two-dimensional background histogram shows number counts of H II regions in PHANGS galaxies; for these regions, a metallicity-dependent α_{CO} was used in the bottom row. At fixed gas column density, PAH emission (left column) in NGC 6822 and WLM is significantly weaker than for H II regions in PHANGS galaxies. Meanwhile the I_ν^{F2100W} vs. N(H I) and I_ν^{F2100W} vs. $N(\mathrm{H_{tot}})$ relationships may be much more similar between PHANGS and NGC 6822 and WLM, but deeper F2100W observations are required to confirm this.

find substantial, ≈0.5 dex, field-to-field variation in NGC 6822 with high values in Field 4 similar to the SMC, and low values in Fields 1–3 similar to WLM. These measurements appear consistent with the well-documented drop in PAH emission at low metallicity found in numerous Spitzer studies.

2. Our observations resolve the H II regions within the larger star-forming complexes. In all four NGC 6822 fields, we observe decreased $I_\nu^{F770W}/I_\nu^{F2100W}$ within the H II regions compared to the surrounding clouds, consistent with PAH destruction in ionized gas. In NGC 6822, we observe a drop of 0.50 dex in the $I_\nu^{F770W}/I_\nu^{F2100W}$ ratio from outside to inside the H II regions (Table 3). This is consistent with the drop in the Spitzer $I_\nu^{IRAC\ 8\,\mu m}/I_\nu^{MIPS\ 24\,\mu m}$ ratio or fitted PAH abundance seen between the neutral and ionized gas in the

Magellanic Clouds and in the drop in PAH abundance measured when contrasting H II regions and diffuse ISM at larger scales in PHANGS-JWST (Figure 6, Table 3, Appendix).

3. Because H II regions still exhibit bright MIR emission, our measured drop in $I_\nu^{\rm F770W}/I_\nu^{\rm F2100W}$ toward their interiors leads to a broken power law when plotting $I_\nu^{\rm F770W}$ versus $I_\nu^{\rm F2100W}$ intensity, with a shallow slope (<1) at high intensities. This relationship appears common among NGC 6822, the Magellanic Clouds, and the PHANGS-JWST galaxies.
4. Within the well-shielded regions with a size of a few parsecs where CO emission is detected in both NGC 6822 and WLM, we observe $I_{\rm CO(2-1)}$-to-$I_\nu^{\rm F770W}$ ratios similar to those observed at 50–100 pc scales in more massive galaxies at higher metallicity. Meanwhile, the $I_{\rm CO(2-1)}$-to-$I_\nu^{\rm F2100W}$ ratio even in these CO-bright regions appears significantly lower in NGC 6822 and WLM than in more massive galaxies. This suggests that CO and PAH emission may be suppressed by comparable amounts at these metallicities, but that the small, stochastically heated dust grains traced by the F2100W filter remain more abundant than CO and PAHs. We emphasize that, on average, only 5%–50% (F770W) and 6%–74% (F2100W) of the MIR emission appears coincident with CO detections and enters this analysis (Table 2). While the ALMA data lack short spacing and sensitivity to compare rigorously to JWST over a wider area, qualitatively both the F770W and F2100W appear more extended than the ALMA CO.
5. While all of our target fields are full of high-column-density 21 cm H I emission, the MIR emission appears more spatially confined, dramatically more so in WLM. Compared to PHANGS galaxies, we observe low $I_\nu^{\rm F2100W}$-to-H I column density ratios and even lower $I_\nu^{\rm F770W}$-to-H I ratios, reflective of a low abundance of small dust grains in the diffuse ISM of NGC 6822 and WLM. In detected apertures in NGC 6822, these ratios appear consistent with being suppressed by factors proportional to the reduced dust-to-gas ratios and PAH abundances in that galaxy, though there are also many apertures where we measure only an upper limit. WLM shows evidence for additional suppression of dust emission relative to these expectations.

These results paint a dynamic picture of the life cycle of small dust grains, PAHs, and gas in galaxies across metallicity. At the same time, these data leave much to be explored in subsequent work, some of which requires new observations, including detailed characterization of point sources, more detailed investigation of the PAH properties (e.g., size and charge), and accounting for the effects of a varying interstellar radiation field within our regions.

Acknowledgments

R.I. acknowledges support from JWST-GO-02130.006-A. V.V. acknowledges support from the ANID BASAL project FB210003. S.C.O.G. acknowledges financial support from the European Research Council via the ERC Synergy Grant "ECOGAL" (project ID 855130) and from the German Excellence Strategy via the Heidelberg Cluster of Excellence (EXC 2181—390900948) "STRUCTURES." J.C. acknowledges funding from the Belgian Science Policy Office (BELSPO) through the PRODEX project "JWST/MIRI Science exploitation" (C4000142239).

This paper makes use of the following ALMA data:ADS/JAO.ALMA#2018.1.00337.S, ADS/JAO.ALMA#2012.1.00336.S, and ADS/JAO.ALMA#2024.1.01179.S. ALMA is a partnership of ESO (representing its member states), NSF (USA) and NINS (Japan), together with NRC (Canada), NSTC and ASIAA (Taiwan), and KASI (Republic of Korea), in cooperation with the Republic of Chile. The Joint ALMA Observatory is operated by ESO, AUI/NRAO and NAOJ.

This work was conducted as part of the Local Group L-Band survey (LGLBS). The LGLBS is an Extra Large program conducted on Jansky Very Large Array, which is operated by the National Radio Astronomy Observatory (NRAO) and includes observations from VLA projects 20A-346, 13A-213, 14A-235, 14B-088, 14B-212, 15A-175, 17B-162, and GBT projects 09A-017, 13A-420, 13A-430, 13B-169, 14A-367, 16A-413.

NRAO is a facility of the National Science Foundation operated under cooperative agreement by Associated Universities, Inc. Execution of the LGLBS survey science was supported by NSF Award 2205628.

We thank the anonymous referee for their timely and helpful feedback.

Facilities: JWST, ALMA, VLA, Spitzer.

Appendix
What $q_{\rm PAH}$ is Implied by Our Measured $I_\nu^{\rm F770W}/I_\nu^{\rm F2100W}$?

We measure variations in $I_\nu^{\rm F770W}/I_\nu^{\rm F2100W}$, which is commonly interpreted as a tracer of fraction of the dust mass in PAHs. Because there are multiple strong PAH features and the far-IR SED, not the MIR, offers the most direct tracer of large dust grain mass, one would ideally prefer to use the ratio of total PAH-to-total IR luminosity or full IR SED modeling to estimate $q_{\rm PAH}$ (B. T. Draine & A. Li 2007, and see F. Galliano et al. 2018; A. Li 2020). Lacking the data required for those approaches, one can still estimate $q_{\rm PAH}$ via $I_\nu^{\rm F770W}/I_\nu^{\rm F2100W}$ given models and assumptions about the interstellar radiation field (ISRF) and dust property distribution. Following similar work in PHANGS by J. Chastenet et al. (2023a) and J. Sutter et al. (2024), here we compare our measured $I_\nu^{\rm F770W}/I_\nu^{\rm F2100W}$ to model calculations by B. T. Draine & A. Li (2007) and B. S. Hensley & B. T. Draine (2023), and to results that fit SED models to measurements with lower physical resolution but more complete wavelength coverage by J. Chastenet et al. (2025).

In Figure 13 we show $q_{\rm PAH}$ as a function of $I_\nu^{\rm F770W}/I_\nu^{\rm F2100W}$, marking the values of $I_\nu^{\rm F770W}/I_\nu^{\rm F2100W}$ measured in our data. Colored solid lines show model curves from B. T. Draine et al. (2007) and B. S. Hensley & B. T. Draine (2023). The left panels illustrate how the $I_\nu^{\rm F770W}/I_\nu^{\rm F2100W}$–$q_{\rm PAH}$ relationship depends on aspects of the ISRF. We vary the diffuse ISRF intensity, $U_{\rm min}$, and the fraction of dust mass illuminated by more intense radiation fields, γ (B. T. Draine & A. Li 2007). The right panel shows the B. S. Hensley & B. T. Draine (2023) models and illustrates the effect of varying the grain size distributions (following the definitions of size distribution of B. T. Draine et al. 2021).

In the left panel, the grayscale shows data density for SED-fitting results where J. Chastenet et al. (2025) fit $q_{\rm PAH}$ based on combined Herschel and Wide-field Infrared Survey Explorer

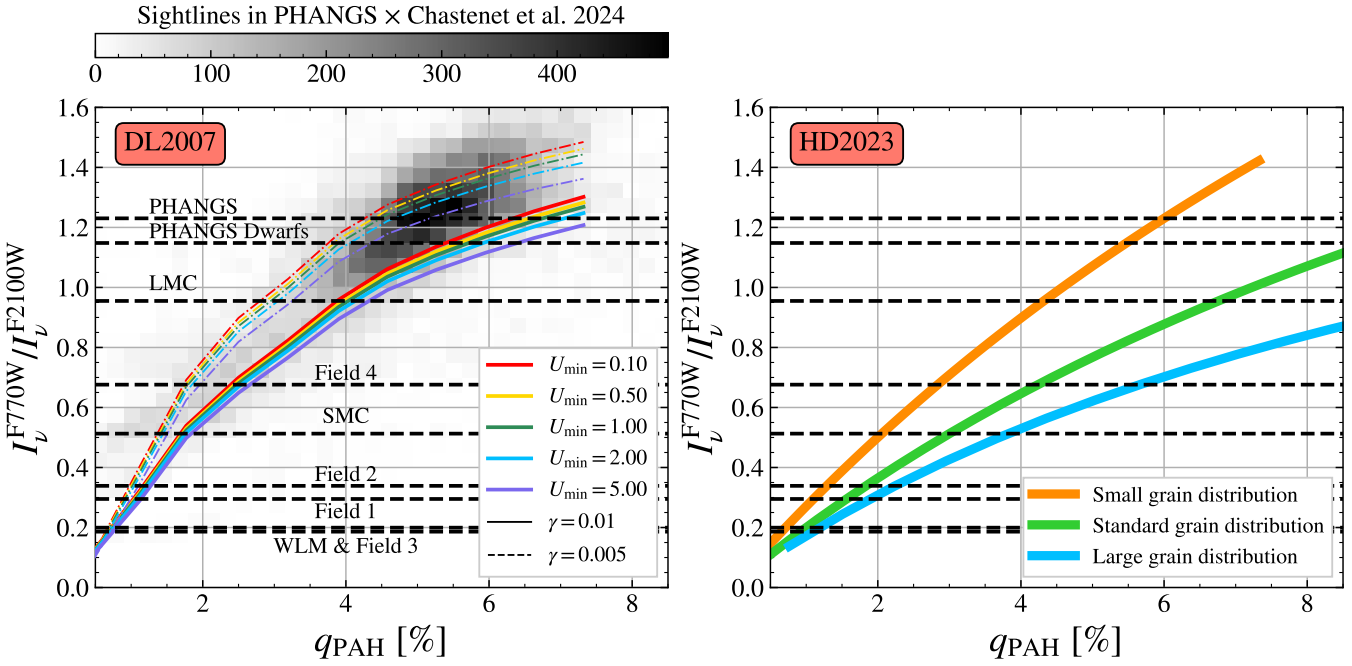

Figure 13. $I_\nu^{\rm F770W}/I_\nu^{\rm F2100W}$ as a function PAH-to-dust mass fraction $q_{\rm PAH}$. The colored curves in the left panel show the B. T. Draine et al. (2007) dust models with varying ISRF distributions ($U_{\rm min}$ is the intensity of the diffuse ISRF, γ indicates the fraction of dust heated by more intense radiation). The curves in the right panel were computed using the B. S. Hensley & B. T. Draine (2023) dust model, which adopts the PAH population from B. T. Draine et al. (2021). The three curves represent the "small," "standard," and "large" grain distributions ($a_{01} = 3$, 4, 5 Å). Grayscale in the left image shows data density for ≈20″ regions in 33 PHANGS targets where J. Chastenet et al. (2025) estimate $q_{\rm PAH}$ from IR SED modeling using the B. T. Draine & A. Li (2007) models and we measure $I_\nu^{\rm F770W}/I_\nu^{\rm F2100W}$ at matched resolution. These therefore give a sense of the $I_\nu^{\rm F770W}/I_\nu^{\rm F2100W}$–$q_{\rm PAH}$ relation for real parts of galaxies for these models. The horizontal lines show the median $I_\nu^{\rm F770W}/I_\nu^{\rm F2100W}$ for samples studied in this paper (Table 3; note that the LMC and SMC show the slightly different $I_\nu^{\rm IRAC\ 8\mu m}/I_\nu^{\rm MIPS\ 24\mu m}$).

data. From their atlas, we selected 34 PHANGS galaxies that also have JWST F770W and F2100W measurements, which we used to measure $I_\nu^{\rm F770W}/I_\nu^{\rm F2100W}$ at resolution matched to J. Chastenet et al. (2025). The grayscale thus gives a practical estimate of how $I_\nu^{\rm F770W}/I_\nu^{\rm F2100W}$ traces model-fit $q_{\rm PAH}$ in real local star-forming galaxies (see also J. Sutter et al. 2024).

Figure 13 shows that the $I_\nu^{\rm F770W}/I_\nu^{\rm F2100W}$ for WLM and NGC 6822 Fields 1, 2, and 3 lies below almost all of the J. Chastenet et al. (2025) comparison data. Comparing to the B. T. Draine et al. (2007) curves or extrapolating the J. Chastenet et al. (2025) trend implies low $q_{\rm PAH}$, of order ≈1% ± 0.5% for these four fields and the B. T. Draine et al. (2007) models. This agrees with previous modeling by B. T. Draine et al. (2007), which found $q_{\rm PAH}$ of 0.7%–1.1% for the integrated SED of NGC 6822 (B. T. Draine et al. 2007). Field 4 shows higher $I_\nu^{\rm F770W}/I_\nu^{\rm F2100W}$ and does overlap some of the J. Chastenet et al. (2025) comparison data. On their system, we would expect this field to have $q_{\rm PAH} \approx 2\% \pm 0.5\%$. For comparison, the typical PHANGS ratio that we measure corresponds to $q_{\rm PAH} \approx 5\% \pm 1\%$ in the J. Chastenet et al. (2025) comparison sample, in good agreement with J. Sutter et al. (2024). We emphasize that these values are still dependent on the physical dust properties assumed, as illustrated by variation between the models in the left and right panels.

These model curves and the comparison to J. Chastenet et al. (2025) consider filter-integrated measurements, which work well given some model framework, but a more empirical path forward is to add up the PAH luminosity from each of the major features rather than just the 7.7 μm feature (i.e., also including the 3.3 μm and 11.3 μm complexes). In environments where PAH emission becomes faint (such as NGC 6822 and WLM), it will also be important for future work to account for contaminants in the filters, including starlight and continuum from small dust grains in the F770W filter and possibly some PAH emission in the F2100W filter. The fractional contributions are most likely strong functions of location, as seen in other sources (e.g., R. Chown et al. 2025b).

ORCID iDs

Ryan Chown https://orcid.org/0000-0001-8241-7704
Adam K. Leroy https://orcid.org/0000-0002-2545-1700
Alberto D. Bolatto https://orcid.org/0000-0002-5480-5686
Jérémy Chastenet https://orcid.org/0000-0002-5235-5589
Simon C. O. Glover https://orcid.org/0000-0001-6708-1317
Rémy Indebetouw https://orcid.org/0000-0002-4663-6827
Eric W. Koch https://orcid.org/0000-0001-9605-780X
Jennifer Donovan Meyer https://orcid.org/0000-0002-3106-7676
Nickolas M. Pingel https://orcid.org/0000-0001-9504-7386
Erik Rosolowsky https://orcid.org/0000-0002-5204-2259
Karin Sandstrom https://orcid.org/0000-0002-4378-8534
Jessica Sutter https://orcid.org/0000-0002-9183-8102
Elizabeth Tarantino https://orcid.org/0000-0003-1356-1096
Frank Bigiel https://orcid.org/0000-0003-0166-9745
Médéric Boquien https://orcid.org/0000-0003-0946-6176
I-Da Chiang (江宜達) https://orcid.org/0000-0003-2551-7148
Daniel A. Dale https://orcid.org/0000-0002-5782-9093
Julianne J. Dalcanton https://orcid.org/0000-0002-1264-2006
Oleg V. Egorov https://orcid.org/0000-0002-4755-118X
Cosima Eibensteiner https://orcid.org/0000-0002-1185-2810

Kathryn Grasha https://orcid.org/0000-0002-3247-5321
Hamid Hassani https://orcid.org/0000-0002-8806-6308
Hao He https://orcid.org/0000-0001-9020-1858
Jaeyeon Kim https://orcid.org/0000-0002-0432-6847
Sharon Meidt https://orcid.org/0000-0002-6118-4048
Debosmita Pathak https://orcid.org/0000-0003-2721-487X
Sumit K. Sarbadhicary https://orcid.org/0000-0002-4781-7291
Snezana Stanimirovic https://orcid.org/0000-0002-3418-7817
Vicente Villanueva https://orcid.org/0000-0002-5877-379X
Thomas G. Williams https://orcid.org/0000-0002-0012-2142

References

Allamandola, L. J., Tielens, A. G. G. M., & Barker, J. R. 1989, ApJS, 71, 733
Archer, H. N., Hunter, D. A., Elmegreen, B. G., et al. 2024, AJ, 167, 274
Belfiore, F., Leroy, A. K., Williams, T. G., et al. 2023, A&A, 678, A129
Bertin, E., & Arnouts, S. 1996, A&AS, 117, 393
Bisbas, T. G., Zhang, Z.-Y., Kyrmanidou, M.-C., et al. 2025, A&A, 697, A115
Bolatto, A. D., Wolfire, M., & Leroy, A. K. 2013, ARA&A, 51, 207
Bushouse, H., Eisenhamer, J., Dencheva, N., et al. 2025, JWST Calibration Pipeline, v1.17.1, Zenodo, doi:10.5281/zenodo.14597407
Cannon, J. M., Walter, F., Armus, L., et al. 2006, ApJ, 652, 1170
Chastenet, J., Sandstrom, K., Chiang, I.-D., et al. 2019, ApJ, 876, 62
Chastenet, J., Sandstrom, K., Leroy, A. K., et al. 2025, ApJS, 276, 2
Chastenet, J., Sutter, J., Sandstrom, K., et al. 2023a, ApJL, 944, L12
Chastenet, J., Sutter, J., Sandstrom, K., et al. 2023b, ApJL, 944, L11
Chiang, I.-D., Sandstrom, K. M., Chastenet, J., et al. 2024, ApJ, 964, 18
Choudhury, S., Subramaniam, A., & Cole, A. A. 2016, MNRAS, 455, 1855
Choudhury, S., Subramaniam, A., Cole, A. A., & Sohn, Y. J. 2018, MNRAS, 475, 4279
Chown, R., Leroy, A. K., Sandstrom, K., et al. 2025a, ApJ, 983, 64
Chown, R., Li, C., Parker, L., et al. 2021, MNRAS, 500, 1261
Chown, R., Okada, Y., Peeters, E., et al. 2025b, A&A, 698, A86
Chown, R., Sidhu, A., Peeters, E., et al. 2024b, A&A, 685, A75
Churchwell, E., Povich, M. S., Allen, D., et al. 2006, ApJ, 649, 759
Churchwell, E., Whitney, B. A., Babler, B. L., et al. 2004, ApJS, 154, 322
Compiègne, M., Abergel, A., Verstraete, L., & Habart, E. 2008, A&A, 491, 797
Cui, Q.-L., Zhang, C.-P., & Wang, J.-J. 2024, RAA, 24, 045023
de Grijs, R., & Bono, G. 2015, AJ, 149, 179
Dicken, D., Marìn, M. G., Shivaei, I., et al. 2024, A&A, 689, A5
Draine, B. T. 2011, Physics of the Interstellar and Intergalactic Medium (Princeton, NJ: Princeton Univ. Press)
Draine, B. T., Dale, D. A., Bendo, G., et al. 2007, ApJ, 663, 866
Draine, B. T., & Li, A. 2007, ApJ, 657, 810
Draine, B. T., Li, A., Hensley, B. S., et al. 2021, ApJ, 917, 3
Efremova, B. V., Bianchi, L., Thilker, D. A., et al. 2011, ApJ, 730, 88
Egorov, O. V., Kreckel, K., Sandstrom, K. M., et al. 2023, ApJL, 944, L16
Emsellem, E., Schinnerer, E., Santoro, F., et al. 2022, A&A, 659, A191
Engelbracht, C. W., Gordon, K. D., Rieke, G. H., et al. 2005, ApJL, 628, L29
Galliano, F., Galametz, M., & Jones, A. P. 2018, ARA&A, 56, 673
Gao, Y., Xiao, T., Li, C., et al. 2019, ApJ, 887, 172
Gaustad, J. E., McCullough, P. R., Rosing, W., & Van Buren, D. 2001, PASP, 113, 1326
Glover, S. C. O., & Clark, P. C. 2012a, MNRAS, 421, 9
Glover, S. C. O., & Clark, P. C. 2012b, MNRAS, 426, 377
Gordon, K. D., Engelbracht, C. W., Rieke, G. H., et al. 2008, ApJ, 682, 336
Gordon, K. D., Meixner, M., Meade, M. R., et al. 2011, AJ, 142, 102
Gratier, P., Braine, J., Rodriguez-Fernandez, N. J., et al. 2010, A&A, 512, A68
Grenier, I. A., Casandjian, J.-M., & Terrier, R. 2005, Sci, 307, 1292
Groves, B., Kreckel, K., Santoro, F., et al. 2023, MNRAS, 520, 4902
Hensley, B. S., & Draine, B. T. 2023, ApJ, 948, 55
Hensley, B. S., Murray, C. E., & Dodici, M. 2022, ApJ, 929, 23
Hernández-Martìnez, L., Peña, M., Carigi, L., & Garcìa-Rojas, J. 2009, A&A, 505, 1027
Hogg, D. W., Tremonti, C. A., Blanton, M. R., et al. 2005, ApJ, 624, 162
Hu, C.-Y., Sternberg, A., & van Dishoeck, E. F. 2021, ApJ, 920, 44
Hu, C.-Y., Sternberg, A., & van Dishoeck, E. F. 2023, ApJ, 952, 140
Hunter, D. A., & Elmegreen, B. G. 2004, AJ, 128, 2170
Hunter, D. A., Elmegreen, B. G., & Ludka, B. C. 2010, AJ, 139, 447
Hunter, D. A., Elmegreen, B. G., & Madden, S. C. 2024, ARA&A, 62, 113
Hunter, D. A., Ficut-Vicas, D., Ashley, T., et al. 2012, AJ, 144, 134
Israel, F. P. 1997, A&A, 328, 471
Jackson, D. C., Cannon, J. M., Skillman, E. D., et al. 2006, ApJ, 646, 192
Jackson, D. C., Skillman, E. D., Cannon, J. M., & Côté, S. 2004, AJ, 128, 1219
Jameson, K. E., Bolatto, A. D., Wolfire, M., et al. 2018, ApJ, 853, 111
Jayasinghe, T., Dixon, D., Povich, M. S., et al. 2019, MNRAS, 488, 1141
Ji, W. G., Zhou, J. J., Esimbek, J., et al. 2012, A&A, 544, A39
Jones, O. C., Nally, C., Habel, N., et al. 2023, NatAs, 7, 694
Kim, C.-G., Ostriker, E. C., Kim, J.-G., et al. 2024, ApJ, 972, 67
Leaman, R., Venn, K. A., Brooks, A. M., et al. 2012, ApJ, 750, 33
Lee, H., Skillman, E. D., & Venn, K. A. 2005, ApJ, 620, 223
Lee, J. C., Sandstrom, K. M., Leroy, A. K., et al. 2023, ApJL, 944, L17
Leroy, A. K., Bolatto, A., Gordon, K., et al. 2011, ApJ, 737, 12
Leroy, A. K., Sandstrom, K., Rosolowsky, E., et al. 2023, ApJL, 944, L9
Leroy, A. K., Schinnerer, E., Hughes, A., et al. 2021, ApJS, 257, 43
Li, A. 2020, NatAs, 4, 339
Li, N., Li, C., Mo, H., et al. 2020, ApJ, 896, 38
Madden, S. C., Cormier, D., Hony, S., et al. 2020, A&A, 643, A141
Madden, S. C., Galliano, F., Jones, A. P., & Sauvage, M. 2006, A&A, 446, 877
Madden, S. C., Rémy-Ruyer, A., Galametz, M., et al. 2013, PASP, 125, 600
Maiolino, R., & Mannucci, F. 2019, A&ARv, 27, 3
Maloney, P., & Black, J. H. 1988, ApJ, 325, 389
Meixner, M., Gordon, K. D., Indebetouw, R., et al. 2006, AJ, 132, 2268
Morrison, J. E., Dicken, D., Argyriou, I., et al. 2023, PASP, 135, 075004
Nally, C., Jones, O. C., Lenkić, L., et al. 2024, MNRAS, 531, 183
Neumann, L., den Brok, J. S., Bigiel, F., et al. 2023, A&A, 675, A104
Oey, M. S., Herrera, C. N., Silich, S., et al. 2017, ApJL, 849, L1
Pathak, D., Leroy, A. K., Thompson, T. A., et al. 2024, AJ, 167, 39
Pietrzyński, G., Graczyk, D., Gallenne, A., et al. 2019, Natur, 567, 200
Pineda, J. L., Langer, W. D., Goldsmith, P. F., et al. 2017, ApJ, 839, 107
Pingel, N. M., Chen, H., Stanimirović, S., et al. 2024, ApJ, 974, 93
Povich, M. S., Stone, J. M., Churchwell, E., et al. 2007, ApJ, 660, 346
Rémy-Ruyer, A., Madden, S. C., Galliano, F., et al. 2014, A&A, 563, A31
Rémy-Ruyer, A., Madden, S. C., Galliano, F., et al. 2015, A&A, 582, A121
Rich, J. A., Persson, S. E., Freedman, W. L., et al. 2014, ApJ, 794, 107
Rigby, J., Perrin, M., McElwain, M., et al. 2023, PASP, 135, 048001
Rousseau-Nepton, L., Martin, R. P., Robert, C., et al. 2019, MNRAS, 489, 5530
Rubio, M., Elmegreen, B. G., Hunter, D. A., et al. 2015, Natur, 525, 218
Russell, S. C., & Dopita, M. A. 1992, ApJ, 384, 508
Saintonge, A., & Catinella, B. 2022, ARA&A, 60, 319
Sandstrom, K. M., Bolatto, A. D., Draine, B. T., Bot, C., & Stanimirović, S. 2010, ApJ, 715, 701
Sandstrom, K. M., Koch, E. W., Leroy, A. K., et al. 2023, ApJL, 944, L8
Schinnerer, E., & Leroy, A. K. 2024, ARA&A, 62, 369
Schruba, A., Leroy, A. K., Kruijssen, J. M. D., et al. 2017, ApJ, 835, 278
Schruba, A., Leroy, A. K., Walter, F., et al. 2011, AJ, 142, 37
Schruba, A., Leroy, A. K., Walter, F., et al. 2012, AJ, 143, 138
Scowcroft, V., Seibert, M., Freedman, W. L., et al. 2016, MNRAS, 459, 1170
Shi, Y., Wang, J., Zhang, Z.-Y., et al. 2015, ApJL, 804, L11
Shi, Y., Wang, J., Zhang, Z.-Y., et al. 2016, NatCo, 7, 13789
Shi, Y., Wang, J., Zhang, Z.-Y., et al. 2020, ApJ, 892, 147
Shivaei, I., & Boogaard, L. A. 2024, A&A, 691, L2
Simpson, R. J., Povich, M. S., Kendrew, S., et al. 2012, MNRAS, 424, 2442
Smith, J. D. T., Draine, B. T., Dale, D. A., et al. 2007, ApJ, 656, 770
Sun, J., Leroy, A. K., Ostriker, E. C., et al. 2020, ApJ, 892, 148
Sun, J., Leroy, A. K., Rosolowsky, E., et al. 2022, AJ, 164, 43
Sutter, J., Sandstrom, K., Chastenet, J., et al. 2024, ApJ, 971, 178
Tielens, A. G. G. M. 2008, ARA&A, 46, 289
Utomo, D., Chiang, I.-D., Leroy, A. K., Sandstrom, K. M., & Chastenet, J. 2019, ApJ, 874, 141
Villanueva, V., Bolatto, A. D., Herrera-Camus, R., et al. 2025, A&A, 695, A202
Watson, C., Corn, T., Churchwell, E. B., et al. 2009, ApJ, 694, 546
Weldrake, D. T. F., de Blok, W. J. G., & Walter, F. 2003, MNRAS, 340, 12
Whitcomb, C. M., Sandstrom, K., Leroy, A., & Smith, J. D. T. 2023a, ApJ, 948, 88
Whitcomb, C. M., Sandstrom, K., & Smith, J.-D. T. 2023b, RNAAS, 7, 38
Whitcomb, C. M., Smith, J. D. T., Sandstrom, K., et al. 2024, ApJ, 974, 20
Williams, T., Egorov, O., Rosolowsky, E., et al. 2023, Physics at High Angular Resolution in Nearby GalaxieS—JWST ("PHANGS-JWST"), STScI/MAST, doi:10.17909/EW88-JT15
Williams, T. G., Lee, J. C., Larson, K. L., et al. 2024, ApJS, 273, 13
Wolfire, M. G., Hollenbach, D., & McKee, C. F. 2010, ApJ, 716, 1191
Zhang, H.-X., Hunter, D. A., Elmegreen, B. G., Gao, Y., & Schruba, A. 2012, AJ, 143, 47